

WHEN TO INTERFERE WITH DARK MATTER? THE IMPACT OF WAVE DYNAMICS ON STATISTICS

ALEX GOUGH^{*1}  AND CORA UHLEMANN^{1,2} 

¹School of Mathematics, Statistics and Physics, Newcastle University, Herschel Building, NE1 7RU Newcastle upon Tyne, U.K. and
²Fakultät für Physik, Universität Bielefeld, Postfach 100131, 33501 Bielefeld, Germany

Version July 18, 2024

ABSTRACT

Ultralight candidates for dark matter can present wavelike features on astrophysical scales. Full wave based simulations of such candidates are currently limited to box sizes of 1–10 Mpc/h on a side, limiting our understanding of the impact of wave dynamics on the scale of the cosmic web. We present a statistical analysis of density fields produced by perturbative forward models in boxes of 128 Mpc/h side length. Our wave-based perturbation theory maintains interference on all scales, and is compared to fluid dynamics of Lagrangian perturbation theory. The impact of suppressed power in the initial conditions and interference effects caused by wave dynamics can then be disentangled. We find that changing the initial conditions captures most of the change in one-point statistics such as the skewness of the density field. However, different environments of the cosmic web, quantified by critical points of the smoothed density, appear to be more sensitive to interference effects sourced by the quantum potential. This suggests that certain large-scale summary statistics may need additional care when studying cosmologies with wavelike dark matter.

1. INTRODUCTION

The current standard model of cosmology consists of cold dark matter and a cosmological constant. This Λ CDM model has been extremely successful at describing cosmological observations across a wide range of length and time scales (Frenk & White 2012; Bull et al. 2016; Planck Collaboration et al. 2020), despite the fundamental nature of dark matter and dark energy remaining unknown. Ongoing and upcoming cosmological surveys such as *Euclid* (Laureijs et al. 2011), Rubin Observatory LSST (Ivezić et al. 2019), and DESI (Levi et al. 2013) will provide an enormous amount of data which will allow precision measurement of cosmological parameters, and provide insight into the fundamental nature of these unknown components.

An alternative to the cold dark matter of Λ CDM which has gained a large amount of attention is dark matter which is fundamentally wavelike on astrophysical or cosmological scales. Such dark matter candidates were originally motivated out of particle physics (Peccei & Quinn 1977; Svrcek & Witten 2006; Arvanitaki et al. 2010; Hui et al. 2017; Jaeckel et al. 2022) though their phenomenology can also act to solve small scale challenges in Λ CDM (Douspis et al. 2019; Di Valentino et al. 2021; Perivolaropoulos & Skara 2022). While a multitude of models exist which can encode self interactions or further degrees of freedom, here we concern ourselves with the simplest fundamentally wavelike dark matter candidate, a non-relativistic, ultralight scalar field, which we will refer to throughout as Fuzzy Dark Matter (FDM). Current constraints on various particle properties of axion models specifically, combining both particle and astrophysical constraints can be found in O’Hare (2020, 2024).

Fully non-linear descriptions of FDM are currently are limited to box sizes of 1–10 Mpc at $z \simeq 3$ for boson masses of $m \sim 10^{-23}$ eV/c² (May & Springel 2021; May & Springel 2023). As such, investigations of the impact

of FDM on larger cosmological scales require approximation techniques which neglect the full dynamics. Many of these techniques rely on modelling only the suppression of power on small scales which is present in the initial conditions of FDM, and neglect the interference effects and role of the quantum potential in the dynamics of the dark matter, an approach that has been dubbed “classical FDM” (Dome et al. 2023; Dome et al. 2023). As such, those interference effects are not fully represented in the final density distribution of the dark matter.

Figure 1 shows a slice of the density field produced from the perturbative forward model used in this work. We can directly see that while classical FDM (the black outlined inset) does produce the overall smoothing seen in the full wave physics case (grey inset), by construction it cannot produce the interference fringes which occur due to the quantum potential. This work aims to investigate how justified such approaches are on large cosmological scales, separating the impact of dynamics and initial conditions on larger scales than can be probed with full numerical simulations. The fine grained pattern in the lower left plot is an artefact of the assignment of particles to the grid in LPT fields. This effect disappears when the density field is smoothed, and becomes less noticeable for higher order mass assignment kernels, as shown in Appendix B.

1.1. Numerical Challenges for FDM

In FDM, a single wavefunction ψ describes the dark matter field of a particle with mass m . This wavefunction evolves according to the cosmological Schrödinger-Poisson equations (Widrow & Kaiser 1993; Guth et al. 2015; Marsh 2016; Hui 2021; Ferreira 2021; O’Hare 2024)

$$i\hbar\partial_t\psi = -\frac{\hbar^2}{2ma^2}\nabla^2\psi + mV_N\psi, \quad (1a)$$

$$\nabla^2V_N = \frac{3\Omega_m^0 H_0^2}{2} \frac{|\psi|^2 - 1}{a}. \quad (1b)$$

*a.gough2@newcastle.ac.uk

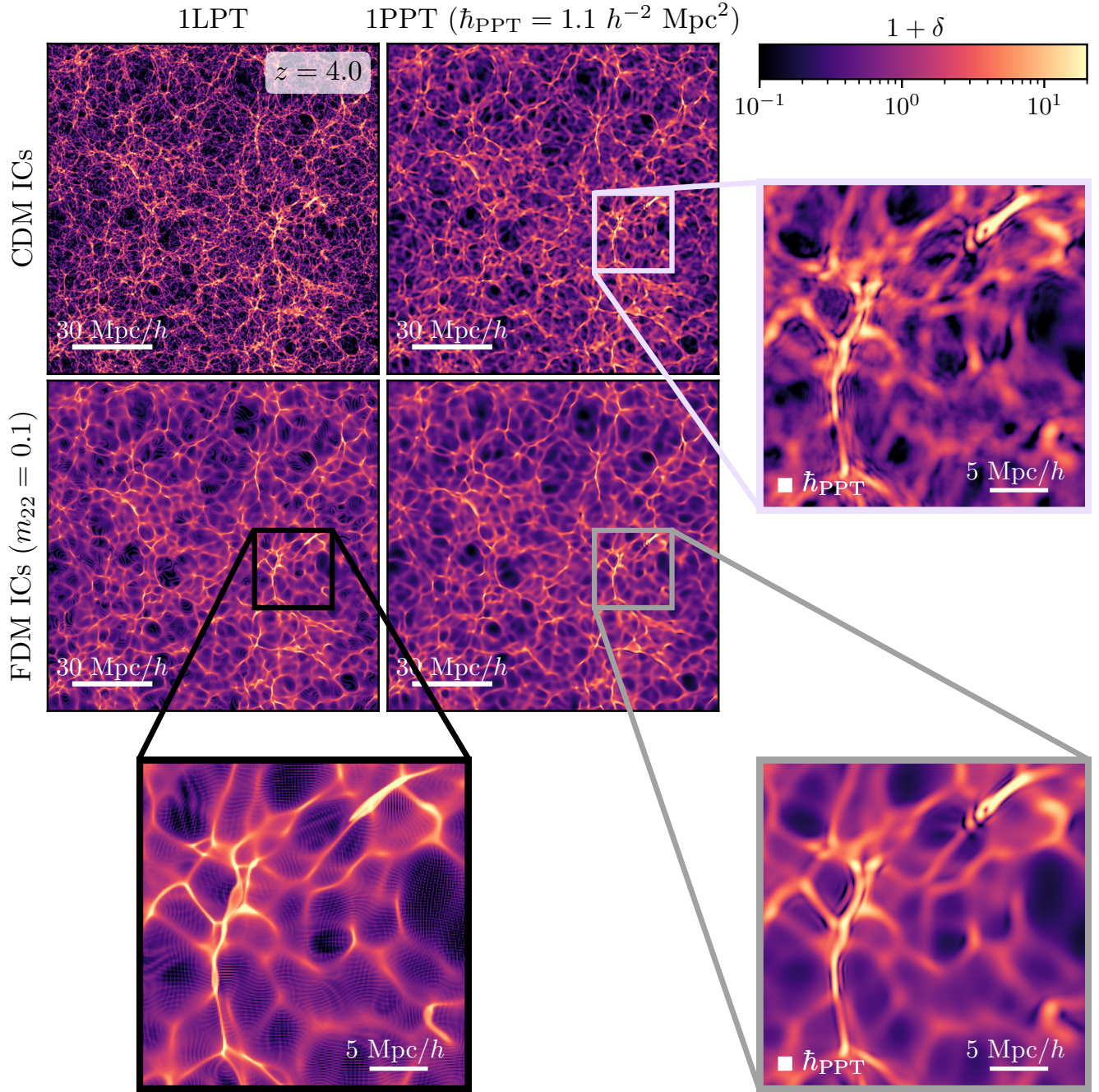


Figure 1. Projected $0.125 \text{ Mpc}/h$ thick slice of the dark matter density field at $z = 4.0$. All plots are shown on the same logarithmic colour scale. These simulations have a box size of $128 \text{ Mpc}/h$ and a grid resolution of $0.125 \text{ Mpc}/h$. The LPT runs traced the positions of $(1024)^3$ particles. The zoomed inset regions are $30 \text{ Mpc}/h$ on a side. The size of the semiclassical parameter \hbar_{PPT} is shown as a white square in the zoomed plots. Columns in the main 2-by-2 correspond to which perturbation theory method is used: classical LPT fluid dynamics or wave PPT dynamics. The rows correspond to the initial conditions, either standard CDM initial conditions, or fuzzy dark matter initial conditions which suppress structure on small scales. The mass for the FDM initial conditions is chosen to be $10^{-23} \text{ eV}/c^2$. Notice that while classical evolution on FDM initial conditions produces a similar large scale cosmic web to the PPT+FDM ICs case, but by construction it cannot produce interference ripples seen in the wave evolution cases.

Here V_N is the Newtonian gravitational potential, Ω_m^0 is the current matter energy density and H_0 is the current Hubble parameter. The wavefunction described here is co-moving, meaning that the physical matter density would scale as $a^{-3/2}$ times this wavefunction. These equations arise as the non-relativistic limit of the Klein-Gordon equation of a scalar field in expanding space, see e.g. [Marsh \(2016\)](#) for a derivation.

The principle challenge in numerically solving the Schrödinger-Poisson equations (1) for the wavefunction while resolving wave interference scales are strict space and time resolution requirements which are dependent on the mass of the FDM particle. For pseudospectral methods such as those used in ([May & Springel 2021](#); [May & Springel 2023](#)) the time step requirement is

$$\Delta t < \min \left(\frac{4}{3\pi} \frac{m}{\hbar} a^2 (\Delta x)^2, 2\pi \frac{\hbar}{m |V_{N,\max}|} \right), \quad (2)$$

where Δx is the spatial resolution and $V_{N,\max}$ is the maximum of the gravitational potential. This is imposed to avoid aliasing in the wavefunction where the phase would increase by more than 2π in adjacent cells. Different numerical schemes will have different exact prescriptions for this form, but all have the scaling that $\Delta t \sim \Delta x^2$ owing to the diffusive nature of the Schrödinger equation. The FDM particle mass itself imposes a restriction on the spatial resolution through its de Broglie wavelength. If we wish to resolve velocities of size v_{\max} in the simulation the spatial grid needs to resolve the de Broglie wavelength associated with that velocity

$$\Delta x < \frac{\hbar}{m v_{\max}} \pi. \quad (3)$$

These joint constraints on Δx and Δt are what make direct, large box, simulations of fuzzy dark matter so computationally expensive, as going to cosmological boxes $\mathcal{O}(100)$ Mpc/ h cannot be achieved by simply decreasing the spatial/temporal resolution.

1.2. Summary of numerical approaches

A variety of different numerical approaches and codes for FDM exist. The most accurate of these are full wavefunction solvers which solve the Schrödinger-Poisson equations for the complex wavefunction e.g. ([Schive et al. 2014](#); [Mocz et al. 2019](#); [May & Springel 2021](#); [May & Springel 2023](#)). [May & Springel \(2021\)](#) examines the impact of changing the dynamics between FDM and N -body CDM simulations (on fixed CDM initial conditions) in 10 Mpc/ h box at $z = 3$ with $m = 0.35 - 0.7 \times 10^{-22}$ eV/ c^2 . [May & Springel \(2023\)](#) extends this analysis to also consider the impact of changing the initial conditions. They find that the initial conditions mostly impact the early evolution of the power spectrum and by $z = 5-3$, non-linear growth has mostly made up for the initial suppression, with the non-linear FDM power spectrum gaining a positive bump on small scales dues to wave interference effects. [Mocz et al. \(2019\)](#) simulates the full dark matter wavefunction together with magneto-hydrodynamic effects in a 1.7 Mpc/ h box down to $z = 5.5$ to study the impact on star formation.

`PyUltraLight` ([Edwards et al. 2018](#)) and `UltraDark.jl` ([Glennon et al. 2023](#)) are also pseudospectral wave solvers. [Guo et al. \(2021\)](#), [Glennon](#)

[et al. \(2023\)](#) and [Luu et al. \(2024\)](#) also describe modelling multiple axion fields, motivated by the fact that the axion-like particles arising from the string axiverse ([Svrcek & Witten 2006](#); [Arvanitaki et al. 2010](#)) generically span a spectrum of masses.

Instead of solving the Schrödinger-Poisson equations for the complex wavefunction, a variety of approaches leverage the fact that the Schrödinger-Poisson equations can be rewritten in the form of hydrodynamical equations and make use of Smoothed Particle Hydrodynamic (SPH) techniques to solve for the fluid variables. Using SPH in this way is advocated for by e.g. ([Mocz & Succi 2015](#); [Marsh 2015](#)). One such code is `AX-GADGET` ([Nori & Baldi 2018](#)), a modification of `GADGET-2` ([Springel 2005](#)) to accommodate for quantum pressure. SPH techniques can reach box lengths of $\sim 50 h^{-1}$ Mpc ([Zhang et al. 2018](#)), but are known to fail getting the details of the interference patterns correct, as the fluid variables become ill behaved in regions of low density ([Mocz & Succi 2015](#); [Veltmaat & Niemeyer 2016](#); [Hopkins 2019](#); [Schwabe & Niemeyer 2022](#)). Different SPH approaches also disagree on the role of the quantum potential with [Nori & Baldi \(2018\)](#) finding that the quantum potential suppresses the matter power spectrum while [Veltmaat & Niemeyer \(2016\)](#) finds enhancement on small scales.

Other techniques use a hybrid approach, such as `AXIONYX` ([Schwabe et al. 2020](#)) that extends the `NYX` code ([Almgren et al. 2013](#)) to solve systems with mixed fuzzy and cold dark matter, solving the FDM component via pseudospectral methods and running N -body for the CDM component. This was recently used in [Laguë et al. \(2024\)](#) for example, which simulates mixed CDM and FDM in 1–30 Mpc/ h boxes, with FDM masses of $10^{-25} - 10^{-21}$ eV/ c^2 . [Schwabe & Niemeyer \(2022\)](#) also take this approach, solving N -body dynamics on large scales and full Schrödinger-Poisson on smaller scales to study individual halos. Both of these methods rely on translating the N -body particles into wavepackets at some point, as discussed in [Gough & Uhlemann \(2022\)](#). The Gaussian beam method was developed with the intention of reconstructing the wavefunction within a collapsed halo. To do this, N -body particles are regarded as phase-space wave-packets and augmented by a complex phase that is co-evolved and coherent between neighbouring wave-packets. As the augmented particles move on classical trajectories, it is similar in spirit to the stationary phase approximation of the propagator [Gough & Uhlemann \(2022\)](#) which assigns classical wavefunctions to individual fluid streams without particle sampling. Both will produce interference effects in classically shell-crossed regions although the details of either method are not guaranteed to be correct compared to a full propagation of the wave-function. Neglecting all wave interference effects, [Dome et al. \(2023\)](#) introduced the term “classical” fuzzy dark matter, where the impact of the FDM is only captured by evolving suppressed initial conditions with standard N -body simulations. This was done in a $40 h^{-1}$ Mpc box between redshifts $z \simeq 3.5-5.5$. As a result the final density fields cannot have interference patterns on any scale as seen in the lower left panel of [Figure 1](#).

1.3. Summary of theoretical approaches

The computational expense of solving the Schrödinger-Poisson equations on cosmological scales has motivated a number of methods to make analytic or perturbative progress on such wavelike systems.

Li et al. (2019) attempts a perturbative expansion directly in the wavefunction $\delta\psi = \psi - \psi_{\text{bgd}}$, however they demonstrate that the requirement that the smallness of $\delta\psi$ generally breaks down before the smallness of fluid variables δ , \mathbf{u} , limiting the applicability of this direct approach.

There are also approaches which are based around modifying modelling tools used in the usual CDM context. Laguë et al. (2021) adjusts the particle displacements from Lagrangian Perturbation Theory (LPT) to account for the fact that linear growth in FDM is scale dependent. This is then applied to models of mixed dark matter. While this incorporates the quantum pressure at the linear level, it neglects non-linear effects in the displacement, as described in Appendix B of Uhlemann et al. (2014), and fails to produce interference fringes in the final density field.

Approaches based on the Effective Field Theory of Large Scale Structure (EFTofLSS) have also been tried, such as in Manouchehri Kousha et al. (2024). These approaches bundle the effects of the wave interference into the counterterms introduced in EFT (such as effective sound speed). This approach however relies on expanding the quantum potential as a series in powers of δ , which breaks down where $\delta = -1$, see the quantum potential term defined in equation (5b). Their simulations also follow the ‘‘classical FDM’’ approach of running N -body simulations on FDM suppressed initial conditions, failing to produce interference effects.

The approach used in this work is Propagator Perturbation Theory (PPT), which perturbatively solves for the propagator which describes how final wavefunctions are constructed from initial wavefunctions in terms of an effective potential. To lowest order, this approach describes free wave propagation in a -time, and at next-to-leading order the effective potential is time-independent, making these equations tractable to solve.

2. WAVELIKE DARK MATTER

In this Section we sketch the relevant cosmological wave equations in this investigation, the true Schrödinger-Poisson equations for an ultralight non-relativistic scalar field and the Schrödinger equations which come out of the Propagator Perturbation formalism.

The de Broglie wavelength of associated to a particle of mass m is given by

$$\lambda_{\text{dB}} = 1.21 \text{ kpc} \left[\frac{10^{-22} \text{ eV}/c^2}{m} \right] \left[\frac{1 \text{ km s}^{-1}}{v} \right], \quad (4)$$

which motivates the definition $m_{22} = m/(10^{-22}\text{eV}/c^2)$ as this sets the de Broglie wavelength on astrophysically relevant scales. Throughout this work we quote masses as values of m_{22} .

2.1. Cosmological Schrödinger-Poisson equations

The Schrödinger-Poisson equations (1) can be recast into fluid-like variables via the Madelung representation

(Madelung 1927), allowing easier comparison to standard CDM dynamics. By writing $\psi = \sqrt{1+\delta}\exp(im\phi/\hbar)$, the Schrödinger-Poisson equations become the continuity equation and a modified Bernoulli equation (Chavanis 2012):

$$\partial_t \delta + \frac{1}{a^2} \nabla \cdot [(1+\delta)\nabla\phi] = 0, \quad (5a)$$

$$\partial_t \phi + \frac{1}{2a^2} |\nabla\phi|^2 = -V_N + \frac{\hbar^2}{2a^2} \frac{\nabla^2 \sqrt{1+\delta}}{\sqrt{1+\delta}}, \quad (5b)$$

$$\nabla^2 V_N = \frac{3\Omega_m^0 H_0^2}{2a} \delta, \quad (5c)$$

where δ is the density contrast and ϕ is the velocity potential which generates the peculiar velocity¹ $\mathbf{u} = d\mathbf{x}/dt = \nabla\phi$. The final term appearing in the Bernoulli equation (5b) is a source of velocity dispersion which doesn’t appear in the equations for a standard fluid, referred to as the ‘‘quantum pressure’’ or ‘‘quantum potential’’.

Linearising these equations in Fourier space leads to a second order equation for δ (Chavanis 2012; Ferreira 2021)

$$\ddot{\delta}_k + 2H(t)\dot{\delta}_k + \left[\left(\frac{\hbar}{m} \frac{k^2}{2a^2} \right)^2 - \frac{3}{2} \Omega_{\text{FDM}}(t) H^2(t) \right] \delta_k = 0, \quad (6)$$

which sets the Jean’s scale as (Chavanis 2012; Marsh 2016)

$$k_J = 66.5a^{1/4} \left(\frac{\Omega_{\text{FDM}}^0 \hbar^2}{0.12} \right)^{1/4} m_{22}^{1/2} \text{ Mpc}^{-1}, \quad (7)$$

where perturbations with $k < k_J$ grow in the linear regime while those with $k > k_J$ oscillate due to the quantum potential balancing against gravity. Solutions to equation (6) determine the linear growth factors $D_{\pm}(k, a)$ for FDM which now no longer factorise into a spatial part and a time dependent part as they did with CDM. The exact growing mode solution to (6) is (Marsh 2016)

$$D_+^{\text{FDM}}(k, a) = \frac{3\sqrt{a}}{\tilde{k}^2} \sin\left(\frac{\tilde{k}^2}{\sqrt{a}}\right) + \left[\frac{3a}{\tilde{k}^4} - 1 \right] \cos\left(\frac{\tilde{k}^2}{\sqrt{a}}\right), \quad (8)$$

where $\tilde{k} = k/\sqrt{mH_0} \propto k/k_J$. In the limit $\tilde{k} \ll 1$ this recovers $D_+^{\text{FDM}} \sim a$ which is the usual CDM growing mode.

2.2. Initial conditions

Adding an additional scalar field to the content of the universe changes the initial conditions which set the linear power spectrum compared to a standard Λ CDM cosmology. The equations which couple the dynamics of this scalar field to the standard fluid content of the universe (CDM, baryons, neutrinos, photons etc) can be found in e.g. Hlozek et al. (2015). For the purposes of structure formation, the principle effect of replacing the cold dark matter with an ultralight field is in the linear matter power spectrum, which is suppressed on small scales.

¹ Note that this is not the typical peculiar velocity $\mathbf{U} = d\mathbf{x}/d\tau = a d\mathbf{x}/dt$.

This suppression is usually quantified relative to the standard CDM power spectrum such that

$$P_{\text{FDM}}(k, z) = T_{\text{FDM}}^2(k, z) P_{\text{CDM}}(k, z). \quad (9)$$

The transfer function $T_{\text{FDM}}(k, z)$ can be approximated by a redshift independent expression (Hu et al. 2000)

$$T_{\text{FDM}}(k) \approx \frac{\cos(x_J^3(k))}{1 + x_J^8(k)}, \quad (10)$$

$$x_J(k) = 1.61 m_{22}^{1/18} k / k_{J,\text{eq}},$$

where $k_{J,\text{eq}} = 9m_{22}^{1/2} \text{Mpc}^{-1}$ is the Jeans scale at matter-radiation equality. Alternatively, the power spectrum of the axion field can be calculated by directly solving the Boltzmann hierarchy with the axion fluid equations included, as in the code `axionCAMB`² (Hlozek et al. 2015).

2.3. Propagator Perturbation Theory

Propagator Perturbation Theory introduces a semiclassical wavefunction ψ to describe the dark matter field, using a semiclassical parameter, \hbar_{PPT} , which controls the amount of wave behaviour in the system, akin to the combination \hbar/m in the FDM scenario. In the semiclassical limit $\hbar_{\text{PPT}} \rightarrow 0$ the dynamics of 1PPT reproduce Zel'dovich approximation (1LPT) dynamics, and can straightforwardly extract quantities in Eulerian space. At higher order, 2PPT produces similar dynamics to 2LPT in the semiclassical limit, but can also protect certain quantities such as the generation of spurious vorticity to higher perturbative order (Uhlemann et al. 2019). PPT was established in Uhlemann et al. (2019), extended to two cold fluids in Rampf et al. (2021); Hahn et al. (2021) and applied as an in the context of generating initial conditions for cosmological simulations in Michaux et al. (2021).

While this formalism is fundamentally based on different underlying physical assumptions than “true” Schrödinger-Poisson/FDM systems discussed above, it does retain non-linear wavelike phenomena in its evolution, rather than relying on classical fluid evolution or simply changing linear growth. Wave interference has certain universal features which even approximate schemes such as PPT can capture (Gough & Uhlemann 2022). Density fields created out of wavefunctions rather than tracer particles are also particularly useful for extracting information from underdense environments such as the Lyman- α forest (Porqueres et al. 2020), due to the wavefunction’s uniform resolution in position space.

The PPT equations are usually written in units such that $4\pi G\bar{\rho}_0 = \frac{3}{2}$ (equivalent to setting $\Omega_m^0 H_0^2 = 1$). Here we keep the physical constants more explicit to aid in mapping between PPT results and more standard PT results.

The dynamical equations of PPT are

$$i\partial_a \hbar_{\text{PPT}} \psi = -\frac{\hbar_{\text{PPT}}^2}{2} \nabla^2 \psi + V_{\text{eff}} \psi, \quad (11a)$$

$$V_{\text{eff}} = \frac{3\Omega_m^0 H_0^2}{2a} (\phi_v + \varphi_g), \quad (11b)$$

$$\nabla^2 \varphi_g = \frac{1}{a} (|\psi|^2 - 1), \quad (11c)$$

² <https://github.com/dgrin1/axionCAMB>

where the effective potential encodes both the gravitational effects and expansion effects through the Hubble drag in the velocity potential ϕ_v .³ It is this effective potential V_{eff} which is solved for perturbatively in PPT. Notice that PPT takes the scale factor a to be its natural time variable, rather than cosmic-time t ⁴ (see Appendix A and Appendix B of Uhlemann et al. (2019) for further discussion of the time variables).

Under the Madelung transformation $\psi = \sqrt{1 + \delta} \exp(i\phi_v/\hbar_{\text{PPT}})$, these equations become the following fluid equations

$$\partial_a \delta + \nabla \cdot [(1 + \delta) \nabla \phi_v] = 0, \quad (12a)$$

$$\partial_a \phi_v + \frac{1}{2} |\nabla \phi_v|^2 = -V_{\text{eff}} + \frac{\hbar_{\text{PPT}}^2}{2} \frac{\nabla^2 \sqrt{1 + \delta}}{\sqrt{1 + \delta}}, \quad (12b)$$

$$\nabla^2 \varphi_g = \frac{\delta}{a}. \quad (12c)$$

The initial conditions for PPT (or LPT) are determined by requiring analytic behaviour at $a = 0$. By considering the fluid equations as $a \rightarrow 0$, the initial conditions for the density contrast and velocity potential are tethered to each other (Brenier et al. 2003)

$$\delta^{(\text{ini})} = 0, \quad \phi_v^{(\text{ini})} = -\varphi_g^{(\text{ini})}. \quad (13)$$

These boundary conditions select for the growing-mode solutions and are vorticity free. In these coordinates, the effective potential becomes very simple. To lowest perturbative order, the effective potential vanishes, making the equations of 1PPT simply a free Schrödinger equation (in a -time). At NLO, the effective potential is non-zero, but is (a)-time independent, making these dynamical equations straightforward to solve.

The free Schrödinger/1PPT dynamics where this effective potential vanishes asymptotically describe the same dynamics as 1st order Lagrangian Perturbation Theory (LPT) or the Zel'dovich approximation (Zel'dovich 1970), where particles are given velocities (relative to a -time) set by the initial gravitational potential, then free stream until shell crossing. This has also been studied as the “free-particle Schrödinger equation” (Coles & Spencer 2003; Short & Coles 2006; Gallagher & Coles 2022). The correspondence of the free wavefunction of 1PPT to Zel'dovich approximation dynamics is explicitly demonstrated in Gough & Uhlemann (2022). Note that within both PPT and LPT vorticity and velocity dispersion will be generated through shell crossing and the formation of multi-streaming regions. In LPT recovering those Eulerian quantities requires an explicit averaging over distinct fluid streams. PPT instead provides direct access to them through the phase information in the wave function, see e.g. Figure 5 in Uhlemann et al. (2019) and Figures 10 and 14 in Gough & Uhlemann (2022). Note that the absence of secondary infall in a single time-step evolution according to LPT and PPT limits the number of attainable fluid streams.

³ Note that we take the sign convention of Gough & Uhlemann (2022) where $\mathbf{v} = \nabla \phi_v$ rather than the convention of Uhlemann et al. (2019) where $\mathbf{v} = -\nabla \phi_v$.

⁴ See Rampf et al. (2021) for generalisation to D -time where D is the linear growth factor.

3. NUMERICAL METHODS FOR PERTURBATIVE FORWARD MODELLING

To examine the effects of initial conditions and evolution dynamics we produce a set of perturbative forward models using a mildly modified version of the initial conditions code `monofonIC`⁵ (Hahn et al. 2021; Michaux et al. 2021). This is intended to generate initial conditions for cosmological simulations using either n LPT to generate particle displacements or n PPT to generate the initial density and velocity fields. For our analysis we run `monofonIC` in 1-fluid mode (dark matter only) with the cosmological parameters shown in Table 1 in a box of $(128 h^{-1} \text{ Mpc})^3$ on a $(1024)^3$ grid. For the LPT runs we run with one particle per grid point. Note that while baryon, radiation, and neutrino fractions are included in Table 1, they are used only in setting the appropriate linear power spectrum, the final output field is dark matter only.

Ω_m	Ω_b	Ω_c	Ω_r	h
0.3158	0.0494	0.264979	7.99185×10^{-5}	0.67321
$\sum m_\nu [\text{eV}/c^2]$	Ω_ν	n_s	A_s	σ_8
0.06	0.001423	0.9661	2.094×10^{-9}	0.8102

Table 1

Cosmological parameters used to produce our density fields with `monofonIC`. We set the value of A_s rather than fixing σ_8 , the value of σ_8 is the extrapolated value at $z = 0$.

The output density fields from `monofonIC` are generated in the following steps:

1. Provide a transfer function for the total matter at the target output redshift $T_m(k, z_t)$ to `monofonIC`.
2. Generate a Gaussian random field with a power spectrum matching the provided target transfer function, call this $\delta_{\text{code}}(\mathbf{x}, a_t)$. As we’re in the perturbative limit, this factorises into $\delta(\mathbf{x}, a) = D_+(a)C_+(\mathbf{x})$. The spatial part of this product is solved by

$$C_+(\mathbf{x}) = \frac{\delta_{\text{code}}(\mathbf{x}, a_t)}{D_+(a_t)}, \quad (14)$$

3. The initial gravitational potential is found by solving the Poisson equation for φ_g then backscaling by the CDM linear growth factor taking the $a \rightarrow 0$ limit

$$\varphi_g^{(\text{ini})}(\mathbf{x}) = \frac{\nabla^{-2} \delta_{\text{code}}}{D_+(a_t)} \lim_{a \rightarrow 0} \frac{D_+(a)}{a}. \quad (15)$$

4. This initial gravitational potential is then used in the relevant PT scheme (either LPT or PPT) to determine the displacement field or the initial wavefunction and effective potential. The perturbative evolutions are then evolved from these initial conditions to the “start redshift” (which will be the final output of this process). In the PPT case the density is constructed as simply $|\psi|^2$ on this grid.

⁵ <https://bitbucket.org/ohahn/monofonic/src/master/>

5. For the classical dynamics (LPT) runs, the density fields are constructed from particle displacements via `Pylians3`⁶ (Villaescusa-Navarro 2018) using the cloud-in-cell mass assignment scheme.

Slices of the final density fields at $z = 4$ are shown in Figure 1. All our output fields have the same fixed target redshift of $z = 4$ and varying “start redshifts”⁷ to investigate the time evolution of certain quantities. All runs which we compare directly are run from the same random seed, providing the same white noise field which is scaled by the target transfer function.

The CDM and FDM linear power spectra which are supplied to `monofonIC` were calculated using `axionCAMB`⁸ (Hlozek et al. 2015), an extension to the standard Boltzmann solver `CAMB` (Lewis & Bridle 2002). As `axionCAMB` requires both axions and standard cold dark matter, the fully CDM/FDM transfer functions were calculated by using an axion fraction of 10^{-7} and $(1 - 10^{-7})$ respectively. These will be referred to as the CDM ICs and FDM ICs throughout. The FDM power spectra were specified with a boson mass of $m_{22} = 0.1$ to accentuate the wave effects on the final field while facilitating a comparison to existing large-scale full FDM simulations (May & Springel 2021; May & Springel 2023).

By default, if `monofonIC` calculates PPT fields, it will choose the minimum value of \hbar_{PPT} that is allowed by the initial gravitational potential to avoid aliasing, in order to match as closely to CDM results as possible. We have modified the `monofonIC` code to allow specification of the size of \hbar which can be larger than this. As `monofonIC` specifies the box size in h^{-1} Mpc units, the value of \hbar_{PPT} is always specified in $(h^{-1} \text{ Mpc})^2$. We choose to run on a fixed size of \hbar_{PPT} which is about 10% larger than the minimum value in the CDM ICs, which ensures that the same \hbar_{PPT} on different random seeds or different initial conditions would also avoid aliasing.⁹

We choose $\hbar_{\text{PPT}} = 1.1 (\text{Mpc}/h)^2$, which has a similar effect on the power spectrum as a boson mass of $m_{22} = 0.1$ on perturbative scales, as shown in Figure 3. As generally \hbar_{PPT} is inversely related to the FDM particle mass, this is the closest \hbar_{PPT} which was feasible to give effects similar to reasonably physical FDM masses. Both parameters \hbar_{PPT} and \hbar/m_{22} control the size of a quantum potential term that is sourced by the curvature of density fluctuations, see equations (5b) and (12b). As they originate from different time and velocity variables, they have a different time-dependence $\hbar_{\text{PPT}}^2 \propto (\hbar/m_{22})^2 a^{-3}$ such that matching their integrated impact depends on the target redshift and the onset of relevance of the quantum potential. We discuss the matching between PPT and FDM in more detail in Appendix A, and present the effect of a larger \hbar_{PPT} in Appendix A.1.

Our choice of a single FDM species with $m_{22} = 0.1$ should be regarded as a toy model that is compatible with constraints from CMB+galaxy clustering (Hlozek

⁶ <https://pylians3.readthedocs.io/en/master/index.html>

⁷ The term “start redshift” is the name given by `monofonIC`, as its standard use is in setting initial conditions for N -body simulations, which would start at z_{start} . When used as a forward model, this “start redshift” is the output redshift of interest, as all the perturbative schemes “start” at $a = 0$.

⁸ <https://github.com/dgrin1/axionCAMB>

⁹ The minimum value of \hbar_{PPT} on the random seed used in this paper was 1.04619 for CDM ICs and 0.987302 on FDM ICs.

et al. 2015; Hložek et al. 2018; Rogers et al. 2023), but incompatible with observations from Lyman-alpha (Iršič et al. 2017; Armengaud et al. 2017; Kobayashi et al. 2017; Rogers et al. 2022, limiting $m_{22} \gtrsim 10$), galaxy UV luminosities (Winch et al. 2024, constraining $m_{22} \gtrsim 0.4$) and ultrafaint dwarf galaxies (Dalal & Kravtsov 2022, constraining $m_{22} \gtrsim 10^3$). Going to higher masses m_{22} requires smaller \hbar_{PPT} , and thus a finer grid at fixed box size thus increasing memory requirements while the perturbative evolution remains computationally cheap. These mass constraints can be relaxed or evaded if FDM makes up only a fraction of the dark matter content (Gosenca et al. 2023; Laguë et al. 2024; Huang et al. 2023) or in the presence of self-interaction terms (Desjacques et al. 2018; Leong et al. 2019; Mocz et al. 2023; Painter et al. 2024). In the context of growing modes in perturbation theory, two dark matter species coupled through the gravitational potential can be realised by imprinting the initial relative densities on to the particle masses (LPT) and the wave function amplitude (PPT), and evolving them with the displacements (LPT) and propagator (PPT) for a single species (in analogy to a two-fluid system with dark matter and baryons discussed in detail in Rampf et al. 2021; Hahn et al. 2021). This could be applied to evolve a mixed CDM and FDM model using a combination of LPT and PPT. Realising mixed FDM models could be achieved by generalising existing results for two-species PPT with a common \hbar_{PPT} to differing $\hbar_{\text{PPT}}^\alpha$ for individual species α .

4. STATISTICS OF THE DENSITY FIELD

In this Section we present statistics measured on the density field produced from `monofonIC` as described above. In principle one could also calculate statistics on the velocity fields predicted with these forward models (directly in LPT and through the wavefunction phase in PPT), which would be a natural extension to this work.

As much as possible we stick to the same colouring scheme for the different statistics investigated in this Section. Colour (or marker shape) is used to differentiate perturbation scheme, representing whether wave dynamics are present or not. The line style is used to differentiate initial conditions, with solid lines for CDM ICs and dashed for FDM ICs. Transparency is used in a few plots to indicate perturbation theory order.

4.1. Power spectrum

The dependence of the power spectrum on initial conditions and dynamics in a full Schrödinger-Poisson solver has been presented in e.g. Figure 6 of May & Springel (2023). In Figure 2 we plot the measured power spectrum at $z = 4$ in a four way comparison between the 1LPT/1PPT dynamics and the CDM/FDM initial conditions, as well as the linear theory power spectra produced by `axionCAMB`. At $z = 4$ the effect of the initial conditions has largely been removed, as non-linear growth has enhanced the initially suppressed power from the FDM initial conditions. Relative to the fully classical evolution (1LPT + CDM ICs, blue solid line) propagation with wave dynamics (orange lines) still features a suppression of power on large scales, owing to the quantum potential term in equation (12b). The vertical lines in Figure 2 indicate a rough region of validity for our

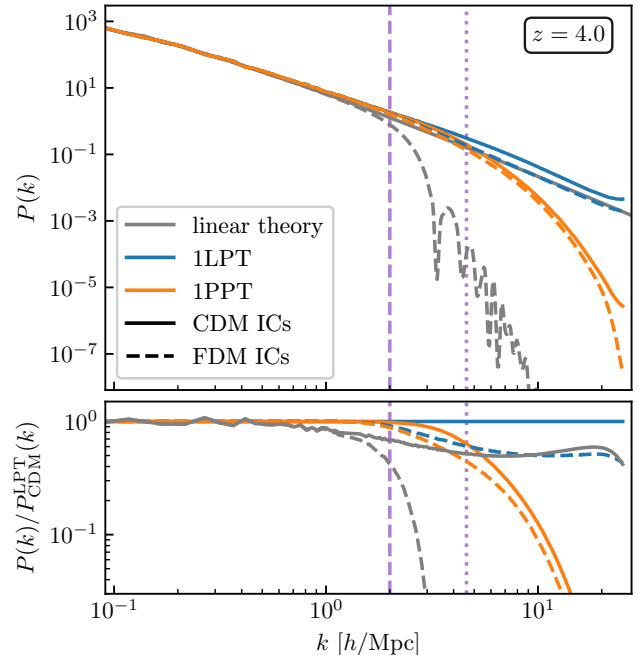


Figure 2. Four way comparison of the power spectrum from 1LPT (CDM) and 1PPT (wave) perturbative simulations with either FDM or CDM initial conditions in a $L = 128 \text{ Mpc}/h$ box. The target linear power spectrum for CDM/FDM is shown as the grey lines. The lower plot shows the ratio of the power spectrum to the classically evolved CDM initial conditions power spectrum. This plot uses the same colouring as Figure 6 in May & Springel (2023) for easy comparison. The dashed vertical line marks the k value where 2LPT produces the most non-linear power compared to 1LPT, and the dotted vertical line denotes the k value beyond which 2LPT produces less power than 1LPT. These provide the bounds on the region of validity for perturbation theory.

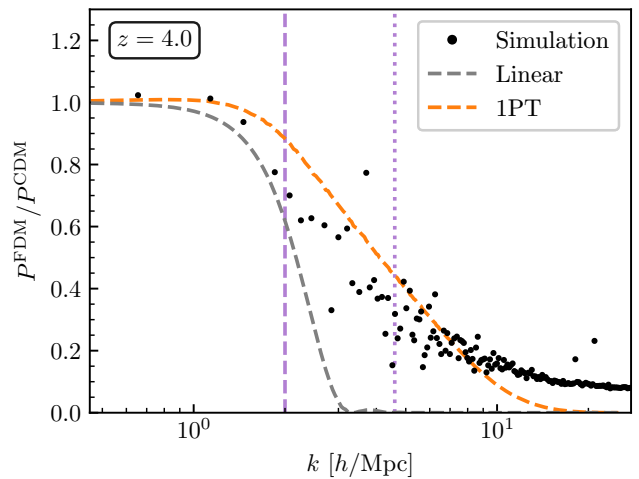


Figure 3. Ratios of the wavelike to classical power spectrum for three cases. First, the ratio of a full Schrödinger-Poisson simulation with suppressed initial conditions ($m_{22} = 0.1$) to an N -body simulation with cold initial conditions (black points, May & Springel 2023). Second, power spectrum from 1PPT + FDM ICs ($\hbar_{\text{PPT}} = 1.1 \text{ (Mpc}/h)^2$, $m_{22} = 0.1$) to 1LPT + CDM ICs (orange dashed). The vertical lines show the relevant perturbative scales as in Figure 2. Third, the linear FDM power spectrum to the linear CDM power spectrum for $m_{22} = 0.1$ (dashed grey).

perturbation theory. The dashed vertical line marks the scale where 2LPT provides the most non-linear power compared to 1LPT, while the dotted vertical line marks the scale where 2LPT produces less non-linear power compared to 1LPT. We see less enhancement over linear power than in the full Schrödinger-Poisson simulations in [May & Springel \(2023\)](#), however the ratio between the power in the fully wave-based and fully classical cases is similar on the scales of interest, as shown in [Figure 3](#).

The ratio between power spectra from fully wave-like and fully classical density fields is used to evaluate whether the chosen value of $\tilde{h}_{\text{PPT}} = 1.1 h^{-2} \text{Mpc}^2$ is well matched to the mass used to set the FDM initial conditions, $m_{22} = 0.1$ in [Figure 3](#). The simulation points are from a full Schrödinger-Poisson simulation with FDM initial conditions (with $m_{22} = 0.1$) in comparison to an N -body simulation with CDM initial conditions from [May & Springel \(2023\)](#). These full simulations were performed in a $10 \text{Mpc}/h$ side length box with $(4320)^3$ grid, the N -body simulation using $(2048)^3$ particles. The relative suppression from perturbation theory with this choice of \tilde{h}_{PPT} slightly underestimates the suppression effect due to wave interference compared to the non-linear simulations. This indicates our choice of $\tilde{h}_{\text{PPT}} = 1.1 h^{-2} \text{Mpc}^2$ represents a conservative estimate of the impact of wave dynamics for a FDM particle mass of $10^{-23} \text{eV}/c^2$. Since the precise mapping between \tilde{h}_{PPT} and the FDM particle mass requires further theoretical understanding (see [Appendix A.3](#) for a discussion and [Appendix A.1](#) for clustering statistics at larger \tilde{h}_{PPT}) we proceed with this choice for the remainder of the analysis, acknowledging that this may underestimate the impact of interference on the density field.

4.2. Matter PDFs and skewness

The distribution of matter density in spheres of radius R is a particularly simple non-Gaussian statistic. We use spherical top-hat filters in real space to smooth the density field, corresponding to the Fourier space window function

$$\begin{aligned} \delta_R(k) &= \tilde{W}(kR)\delta(k), \\ \tilde{W}(kR) &= \frac{3}{(kR)^3} (\sin(kR) - kR \cos(kR)). \end{aligned} \quad (16)$$

The matter PDF in with top-hat smoothing is well modelled in the quasilinear regime by large deviations theory ([Bernardeau et al. 2014](#); [Uhlemann et al. 2016](#)) valid for a wide range of cosmologies even beyond ΛCDM ([Uhlemann et al. 2020](#); [Cataneo et al. 2022](#)).

[Figure 4](#) shows the PDF of the rareriness of the density $\nu = \delta/\sigma$ and the log-density $\mu = \log(1 + \delta)$ while varying the evolution dynamics and the initial conditions in spheres of radius $R = 1 h^{-1} \text{Mpc}$ (8 times the grid scale). As changing the initial conditions changes the final variance on scale R , by plotting the PDF of the rareriness the PDFs are normalised to have the same width. After normalising the width of the PDF it becomes evident that the FDM IC simulations (dashed lines) have an additional skewness compared to the simulations run on CDM initial conditions at $R = 1 h^{-1} \text{Mpc}$. Changing the dynamics on this scale doesn't have a large impact, with the main impact being produced by changing the initial conditions.

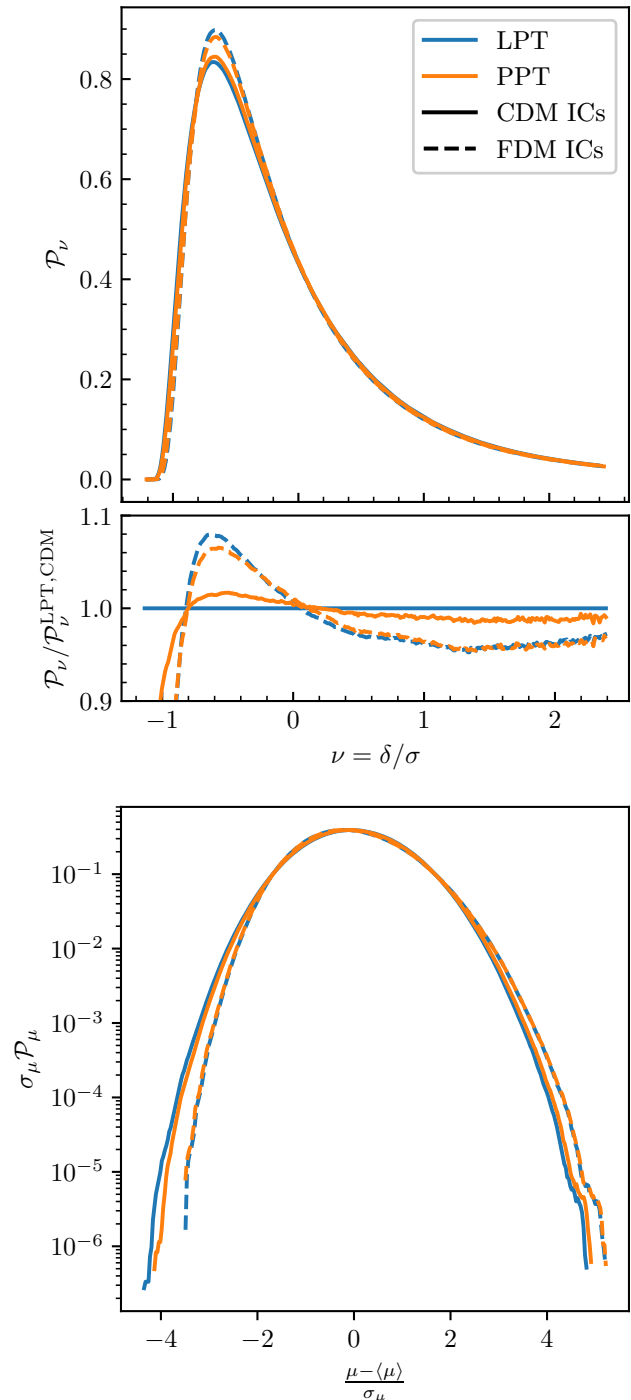


Figure 4. Four way comparison for the matter PDF in spheres of $R = 1 h^{-1} \text{Mpc}$ at $z = 4$. (Top panel) The PDF of the rarity $\nu = \delta_R/\sigma(R)$ where $\sigma^2(R)$ is the variance of the density field on scale R . (Middle panel) The ratio of the rarity PDFs to the fully classical (LPT + CDM ICs) PDF. (Bottom panel) The PDF of the rarity relative to the log density $\mu = \log(1 + \delta)$. Note that suppressed initial conditions (dashed lines) introduce additional skewness to the PDF.

The skewness seen in these PDFs can be well predicted by perturbation theory in terms of the variance. The

reduced cumulants

$$S_n = \frac{\langle \delta^n \rangle_c}{\langle \delta^2 \rangle_c^{n-1}}, \quad (17)$$

are particularly robust hierarchical ratios (Bernardeau 1994a; Bernardeau et al. 2002). In the case of an unsmoothed density field and an EdS universe the reduced cumulants are constant to tree order in standard perturbation theory. When smoothed with a top-hat filter, the reduced cumulants acquire a correction which depends only on the linear variance. SPT predicts the reduced skewness $S_3(R)$ (Bernardeau 1994b)

$$S_3^{\text{tree,SPT}}(R) = \frac{34}{7} + \frac{d \log \sigma_L^2(R)}{d \log R}. \quad (18)$$

However, as the density fields considered in our analysis are not full non-linear simulations the recovered reduced skewness will differ from this value, owing to the difference in dynamics. It is known that n LPT only accurately reproduces cumulants up to S_{n+1} (Munshi et al. 1994). The calculation for reduced skewness can be adapted to the Zel'dovich approximations/1LPT by replacing the 2nd order perturbation kernel $F_2^{\text{SPT}} \rightarrow F_2^{\text{ZA}}$ in the calculation of $\langle \delta_R^3 \rangle$ where (Scoccimarro & Frieman 1996)

$$F_2^{\text{SPT}}(\mathbf{k}_1, \mathbf{k}_2) = \frac{5}{7} + \frac{1}{2} \frac{\mathbf{k}_1 \cdot \mathbf{k}_2}{k_1 k_2} \left(\frac{k_1}{k_2} + \frac{k_2}{k_1} \right) + \frac{2}{7} \frac{(\mathbf{k}_1 \cdot \mathbf{k}_2)^2}{k_1^2 k_2^2}, \quad (19)$$

$$F_2^{\text{ZA}}(\mathbf{k}_1, \mathbf{k}_2) = \frac{1}{2} \frac{(\mathbf{k}_1 + \mathbf{k}_2) \cdot (\mathbf{k}_1 + \mathbf{k}_2)}{k_1^2 k_2^2}. \quad (20)$$

This replacement does not affect the smoothing term, only the bare value of the skewness, leading to (Bernardeau & Kofman 1995)

$$S_3^{\text{tree,ZA}}(R) = 4 + \frac{d \log \sigma_L^2(R)}{d \log R}. \quad (21)$$

This result can also be derived via vertex generating functions (Bernardeau & Kofman 1995). As the linear variance is an integral over the linear power spectrum

$$\sigma_L^2(R) = \int \frac{dk}{2\pi^2} W(kR)^2 P_L(k), \quad (22)$$

the variance for the field run on FDM initial conditions at a fixed physical scale R will be smaller than the variance in the field run on CDM due to the suppression in linear power.

Figure 5 shows the measured reduced skewness against the measured variance $\sigma^2(R)$ on physical scales between 1–10 Mpc/h. The paler lines/open symbols show that the 2nd order PT simulations recover the vertical shift corresponding to $S_3^{\text{tree,SPT}} = 34/7$ instead of the $S_3^{\text{tree,ZA}} = 4$. We see also that on small scales (higher variance) the FDM initial conditions produce a higher reduced skewness, as anticipated from the PDFs in Figure 4. While the standard deviation across subboxes of the simulation is (as indicated by the errorbars) is comparable with this enhancement, the ratio to the LPT+CDM ICs simulation is more robust, indicating that while the entire S_3 line has scatter comparable to the errorbars shown across realisations, the relative enhancement seen

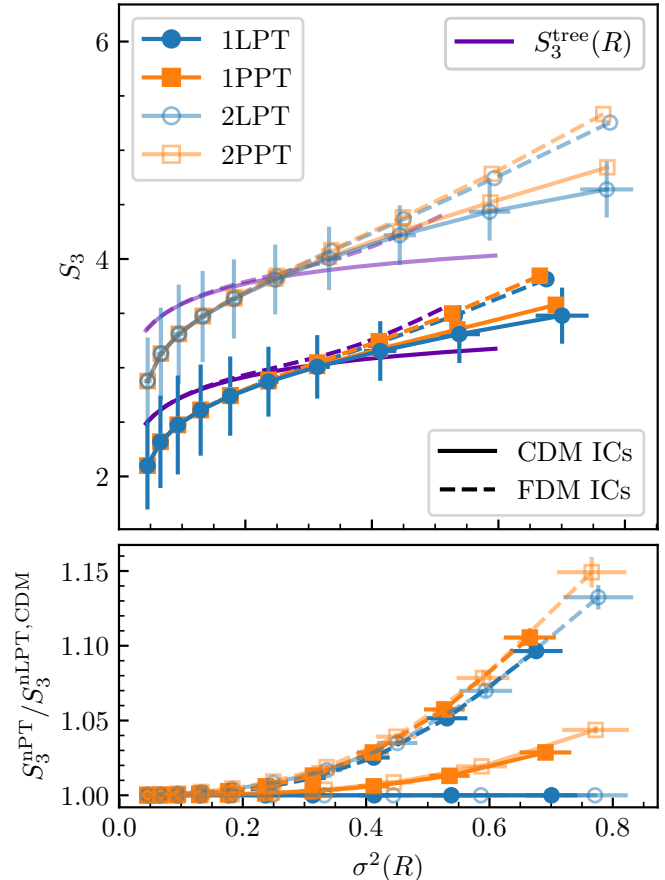


Figure 5. (Top panel) Reduced skewness as a function of variance at $z = 4$, measured on top-hat smoothing scales 1–10 h^{-1} Mpc, log-spaced in R . Paler lines/open symbols show the results from 2nd order PT. The error bars are the standard deviation of the measured quantities across 8 subboxes. The errors are only shown on one line on the top plot to reduce clutter, but errors on other lines are similar. While the errors are relatively large (comparable with the scatter from measuring this across different realisations), the relative splitting (shown in the lower panels) have smaller scatter across realisations, demonstrating that wave effects generally enhance S_3 compared to LPT and CDM, in both smoothing ICs and dynamics. The purple lines (with no markers) are the tree order predictions for $S_3(R)$, which depend only on the linear variance.

is not simply numerical noise. However we can see that the enhancement in S_3 due to the initial conditions appears to be in line with the amount of enhancement anticipated from the smoothing term $d \log \sigma_L^2 / d \log R$. This means that the change in the skewness is largely captured by the change in the suppression from the change in the linear power spectrum. There is a small enhancement to the skewness by introducing wave dynamics but this is subdominant to the change in the overall variance from the initial conditions. This agrees with the findings of Dome et al. (2023) in their classical FDM simulations, where they find simulations with higher suppression in their initial conditions have higher values of S_3 , even on scales significantly smaller than considered here.

The enhancement of non-Gaussian features such as the (reduced) skewness for fields with less small scale power is expected by considering the dynamics of the smoothed

density field in Lagrangian space (Bernardeau 1994a; Bernardeau & Kofman 1995). At a fixed smoothing scale R , regions which are overdense in the final field evolved from larger regions via collapse, while underdense grow from smaller regions. Thus in fields with less small scale power, this asymmetry between over- and underdense regions is stronger than fields with power on small scales, enhancing the skewness as seen. This effect is similar to changing the effective tilt in the primordial power spectrum, as for a linear power spectrum $P_L(k) \propto k^n$, the tree order skewness becomes

$$S_3^{\text{tree}}(R) = S_3^{\text{tree}}(0) + n(R). \quad (23)$$

The removal of small scale power by smoothing on order Mpc scales is known to improve the accuracy of the Zel'dovich approximation by reducing the amount of shell crossing, known as the *truncated Zel'dovich approximation* (Melott et al. 1994).

From the matter PDF and the reduced skewness it appears that the averaging of the density in cells efficiently erases most of the dynamical difference between LPT and PPT, at least in this perturbative regime. However, exactly how strongly separated the dynamical and initial condition effects on S_3 are in PPT depends on understanding the \bar{h}_{PPT} to mass mapping better, as a larger \bar{h}_{PPT} can cause enhancement similar to the FDM initial conditions even from cold initial conditions, generating the skewness purely through dynamics (see Appendix A.1).

4.3. Critical points of the density field

Elements of the cosmic web can be defined and identified in a variety of ways. These elements are usually referred to by their visual nature, knots/peaks for the compact and densest points, line like filaments which extend in one dimension, and sheets or walls which bound the underdense voids. The NEXUS/NEXUS+ algorithm (Cautun et al. 2013) assigns a cosmic web element to every point in a volume a classification based on multiscale analysis of the Hessian of cosmic fields. This was applied in the context of classical FDM in Dome et al. (2023). Classifications based on different fields, such as the tidal or velocity shear fields give rise to the cosmic T-web (Forero-Romero et al. 2009; Ayçoberry et al. 2023) and V-web (Hoffman et al. 2012; Cui et al. 2018). Other classifications include identifying persistent topological structures via Morse methods (Colombi et al. 2000; Sousbie 2011; Sousbie et al. 2011), segmenting the density field (the SpineWeb formalism, Aragón-Calvo et al. 2010), and counting phase space folds (the ORIGAMI method, Falck et al. 2012).

For our purposes we concern ourselves with critical points of the smoothed density field, δ_R .¹⁰ The Hessian matrix of the smoothed density field

$$H_{ij}(\mathbf{x}) = \nabla_i \nabla_j \delta_R(\mathbf{x}), \quad (24)$$

encodes the curvature of the density field in 3 dimensions. Critical points of the density field (defined by $\nabla \delta_R(\mathbf{x}_c) = 0$), can be classified by the number of positive

¹⁰ In this Section we continue to smooth the density field with spherical top-hat filters, as in the previous section. This is in contrast to many other critical point studies which use a Gaussian smoothing filter.

eigenvalues of H at that point, leading to the classification (schematically represented in Figure 6):

- 0 positive eigenvalues, Peak/Node/Knot
- 1 positive eigenvalues, Filament
- 2 positive eigenvalues, Wall
- 3 positive eigenvalues, Void

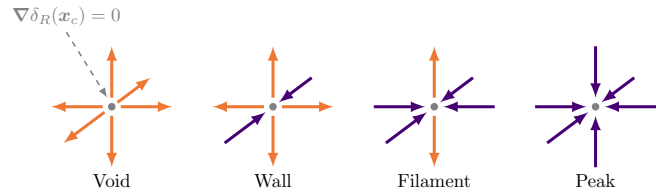


Figure 6. Classification of cosmic web elements via critical points of the smoothed density field. The directions/colours of the arrows indicate the sign of the eigenvalues λ of the Hessian matrix H_{ij} evaluated at the critical point. Outwards/orange arrows correspond to $\lambda > 0$ while inwards/purple arrows correspond to $\lambda < 0$.

Note that in other critical point analyses (e.g. Forero-Romero et al. 2009; Hoffman et al. 2012; Carlesi et al. 2014; Cui et al. 2018; Libeskind et al. 2018; Suárez-Pérez et al. 2021; Ayçoberry et al. 2023) a small non-zero threshold for the eigenvalues of the relevant matrix is used for better visual agreement between the field and the located cosmic web elements.

We run the extrema finding code `py_extrema`¹¹ (Shim et al. 2021), see also Appendix G of Gay et al. (2012)) on the density fields produced by `monofonIC` after smoothing. This calculates the derivatives and Hessian of the smoothed density field in Fourier space and then discards multiple critical points of the same kind which are found to lie in the same pixel. As the derivatives are calculated in Fourier space and require periodic boundary conditions we have to compute them on the full field. The smoothed density field is downsampled from a $(1024)^3$ grid to $(256)^3$ grid before searching for critical points for memory reasons. The density fields used in this Section produced with 1LPT/1PPT with CDM and FDM initial conditions.

4.3.1. Total number of critical points

Figure 7 shows the evolution of the total number of critical points over time, Figure 8 shows the total number of critical points on different smoothing scales at redshift $z = 4$. We see that at all redshifts, any amount of smoothing in the density field, whether from initial conditions or introducing wave dynamics decreases the total number of critical points. This is mirrored as the smoothing scale is increased, which also decreases the total number of critical points. However for radii larger than about $1 h^{-1}$ Mpc, the ratio of number of critical points in the different simulation runs remains roughly constant. We additionally see a stronger redshift evolution of the number of critical points in classical dynamics compared to wave dynamics. Higher amounts of smoothing decrease the total number of critical points, however

¹¹ https://github.com/cphyc/py_extrema

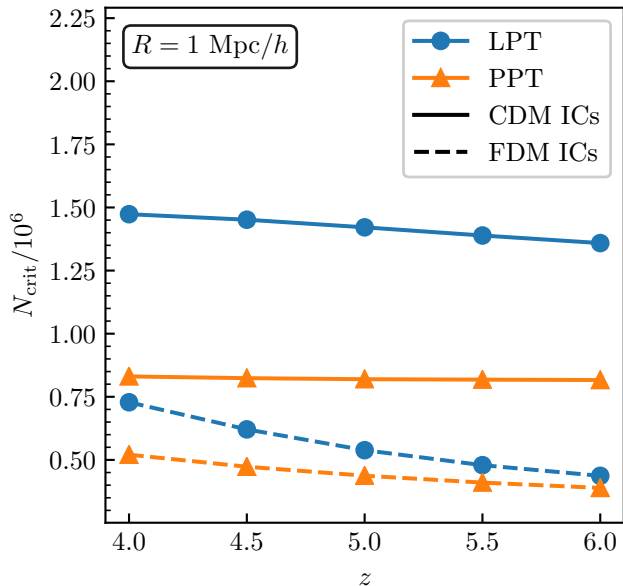


Figure 7. Total number of critical points on the density field smoothed on $R = 1 \text{ Mpc}/h$ as a function of redshift.

the relative fraction of different critical points do not all decrease at the same rate, as we see reflected in the ratios and number fractions between different types of critical points in Figures 9 & 10.

We note as well that the effect of the dynamics (LPT vs PPT, blue vs orange) in this case is stronger than seen in the one-point statistics on the same scale. While the change to the initial conditions provides the bulk of the suppression in the number of critical points, there is a larger separation between the LPT+FDM ICs (blue dashed) and PPT+FDM ICs (orange dashed) cases than seen in the reduced skewness in Figure 5, indicating that critical points are more sensitive to wave interference effects, as expected from a probe of derivatives of the density field.

4.3.2. Fraction of cosmic web elements

In a Gaussian random field the ratio of critical points of different kinds is exactly solvable. The number of peaks and voids (or filaments and walls) are equal, while the ratio of filaments to peaks (or walls to voids) is (Bardeen et al. 1986)

$$\frac{N_{\mathcal{P}}^{\text{G}}}{N_{\mathcal{V}}^{\text{G}}} = \frac{N_{\mathcal{F}}^{\text{G}}}{N_{\mathcal{W}}^{\text{G}}} = 1, \quad (25a)$$

$$\frac{N_{\mathcal{F}}^{\text{G}}}{N_{\mathcal{P}}^{\text{G}}} = \frac{N_{\mathcal{W}}^{\text{G}}}{N_{\mathcal{V}}^{\text{G}}} = \frac{29\sqrt{15} + 18\sqrt{10}}{29\sqrt{15} - 18\sqrt{10}}, \quad (25b)$$

and therefore, the number fractions for a Gaussian random field $f_i^{\text{G}} = N_i^{\text{G}}/N_{\text{crit}}^{\text{G}}$ are

$$f_{\mathcal{P},\mathcal{V}}^{\text{G}} = \frac{29 - 6\sqrt{6}}{116} \approx 12.3\%, \quad (26a)$$

$$f_{\mathcal{F},\mathcal{W}}^{\text{G}} = \frac{29 + 6\sqrt{6}}{116} \approx 37.7\%. \quad (26b)$$

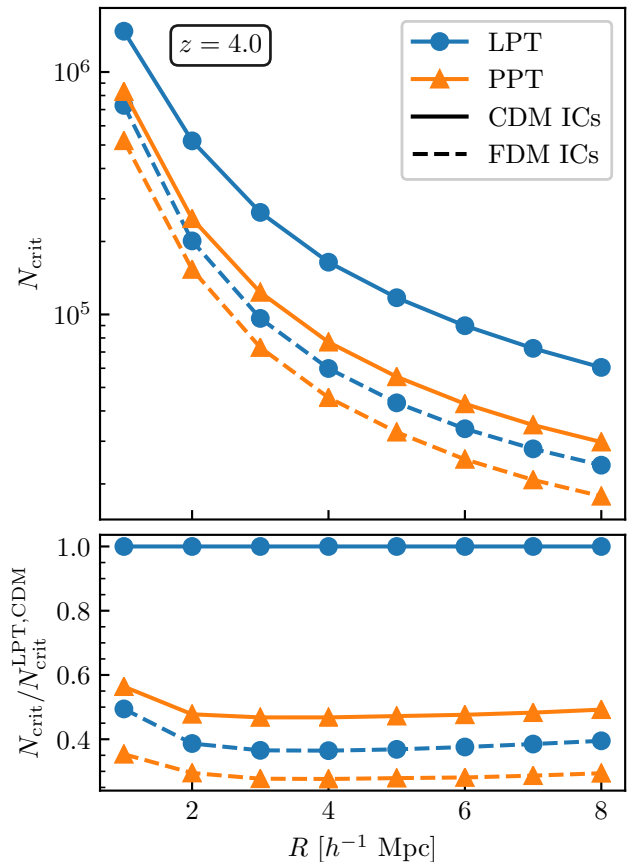


Figure 8. Total number of critical points at $z = 4$ as a function of top-hat smoothing scale R . The lower panel shows the ratio to the number of critical points in the LPT + CDM ICs simulation, which is roughly constant on scales larger than $1 h^{-1} \text{ Mpc}$. The error on the mean based on 8 subboxes is smaller than the marker size in all panels.

Figure 9 shows these ratios as measured on $R = 1 h^{-1} \text{ Mpc}$ together with the Gaussian random field values. We see that generally the fully classical (LPT + CDM ICs) systems are the closer to the Gaussian ratios, with either FDM ICs or wave dynamics introducing higher deviation from the Gaussian ratios. This is consistent with the skewness results, which indicate that FDM initial conditions and wave dynamics both act to produce a more non-Gaussian field, though the dynamical effects have a stronger impact on the non-Gaussianity as measured from the critical points than the skewness.

Figure 10 shows the evolution of the fraction critical points in $1 h^{-1} \text{ Mpc}$ spheres of different types across the different cosmologies.

We see that at all redshifts and for all of the cosmologies, the underdense type critical points (voids and walls) are both enhanced from the fractions which would be expected in a Gaussian field ($\sim 12\%$ for voids and $\sim 38\%$ for walls) with smoothed initial conditions particularly enhancing this enhancement. While we only show the results for 1LPT/1PPT in Figure 10, the same behaviour is seen in the 2nd order perturbative results as well.

From these individual number fractions, we see that

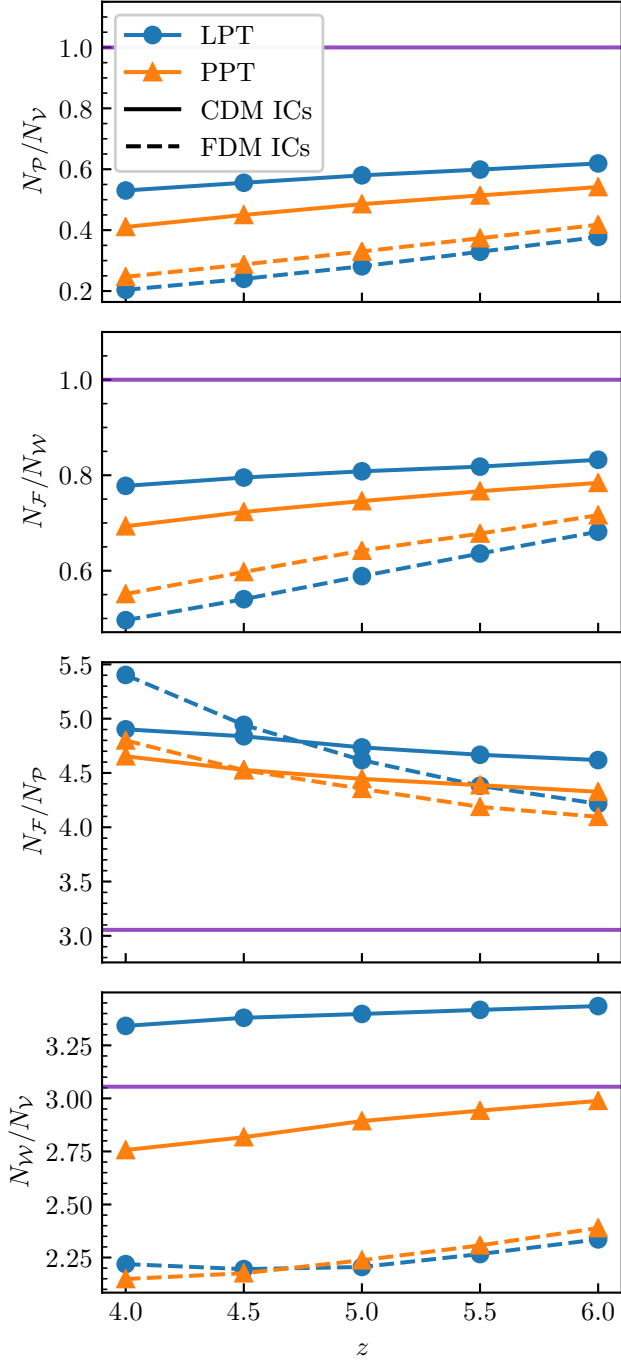


Figure 9. Ratio of number of critical points of different types. The horizontal solid purple lines show the ratios for a Gaussian random field.

while the FDM ICs or PPT dynamics cases produce fewer critical points than the fully classical case, as seen in Figures 7 and 8, the decrease is not uniform across different types of critical points. We see from Figure 10 that underdense type critical points (voids and walls) are pushed further from their Gaussian predicted values than filaments and peaks. This can be explained by two effects. The removal of power on small scales in the FDM

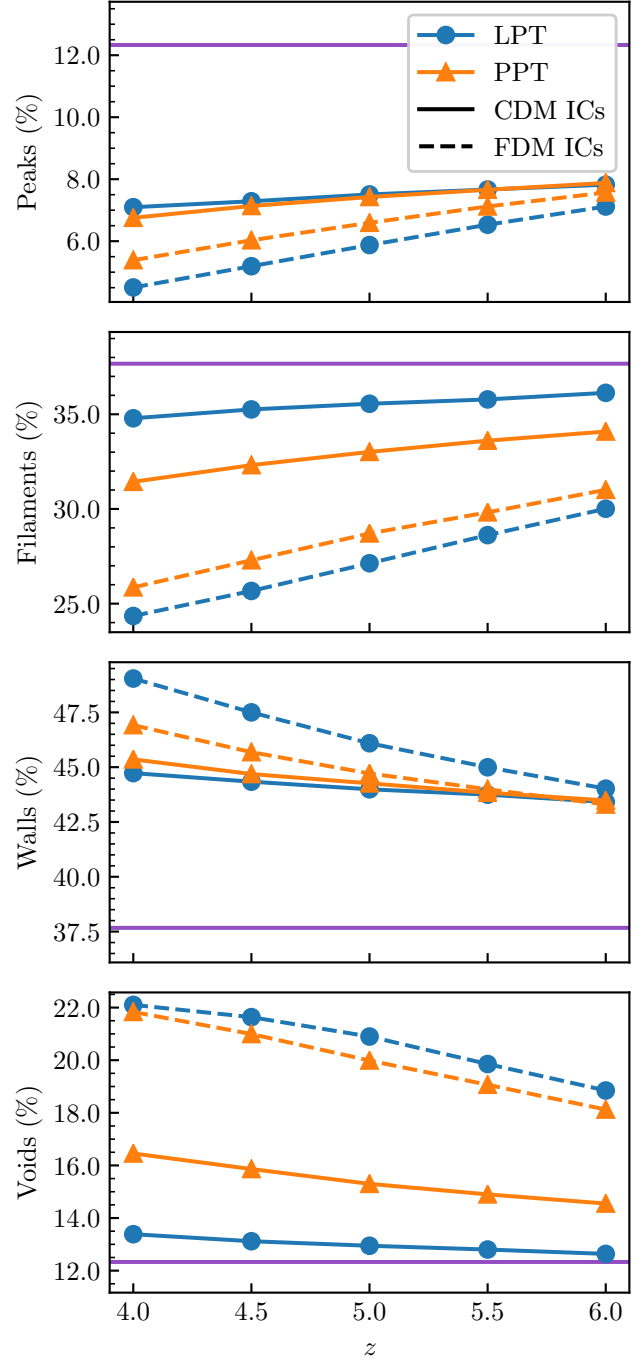


Figure 10. Evolution of the fraction of critical points on $R = 1 h^{-1} \text{ Mpc}$ of a given type. The horizontal solid purple lines show the fraction for a Gaussian random field. Both wave dynamics (orange) and FDM initial conditions (dashed lines) move these fractions further from their Gaussian values.

ICs cases reduces the gravitational potential, making it more difficult for structures to collapse in the first place, preferentially making void and wall type critical points more abundant over filaments and peaks. Secondly, the quantum pressure term in the wave dynamics case (equation 12a) acts to reduce shell crossing compared to the LPT dynamics case, which reduces the overdense type

critical points more.

We note that [Dome et al. \(2023\)](#) examined the mass and volume fractions of different cosmic web elements in the context of classical FDM (analogous to our LPT + FDM ICs case) and found that their volume fraction of voids decreased as the initial conditions were suppressed, contrary to our findings here. However, their cosmic web classification uses the NEXUS+ algorithm to classify all points into a cosmic web element, based on the signs of the Hessian over a range of scales, rather than critical points specifically, so direct comparison of these results is difficult. Much of their analysis also takes place on significantly smaller scales ($\sim 39 h^{-1}$ kpc, their grid scale) than we consider, where more non-linear dynamics is relevant.

4.3.3. Environment spilt PDFs

In addition to the number of critical points of certain types we can also examine the mass distribution of different critical points. Figure 11 shows the overdensity PDFs for different critical point environments $z = 4$ on $R = 1 h^{-1}$ Mpc scales in the fully classical (LPT + CDM initial conditions) density field. We see that as expected,

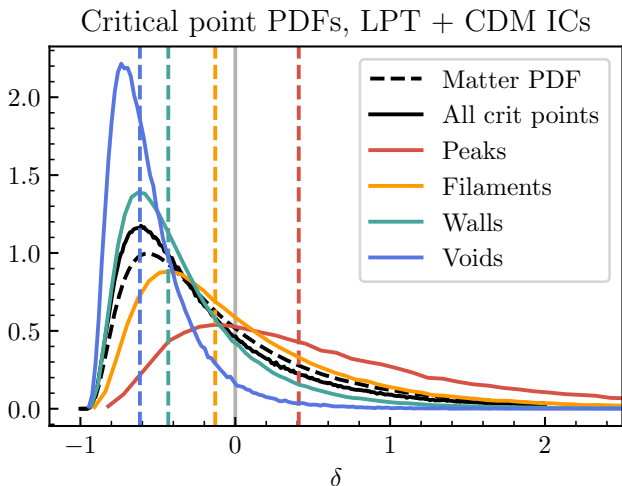


Figure 11. The PDFs of the overdensity of different critical points of the fully classical (LPT + CDM initial conditions) density field at $z = 4$ when smoothed on $R = 1$ Mpc/ h . Each individual PDF is normalised. The PDF of the entire matter field (black dashed), and of all critical points (black solid) are shown for comparison. Coloured vertical lines show the median overdensity for the critical points of that type. The grey vertical line divides over- and underdense regions.

peaks are the densest critical points, while voids are the most underdense. We see the variation of these PDFs across cosmologies in Figure 12. We see that wave dynamics and FDM ICs both increase the density of peaks, shifting the PDFs to the right. Interestingly, while the number of voids was heavily impacted by introducing FDM ICs or wave dynamics, as seen in Figure 10, the void PDF is relatively stable compared to the other environment changes. These effects can be understood by the effect of the quantum potential,

$$Q = -\frac{\hbar_{\text{PPT}}^2}{2} \frac{\nabla^2 \sqrt{1+\delta}}{\sqrt{1+\delta}}, \quad (27)$$

as it is dependent on the curvature of the (square root) of the density, and therefore is largest in regions of high curvature. We see that for cold initial conditions (solid lines) the critical points involving more shell crossing have larger shifts to their PDFs due to this quantum pressure. However, on FDM initial conditions, the PDFs of critical point environments seem less sensitive to the role of this quantum potential, even in the peaks where it was previously the strongest. We expect this is due to the suppressed initial conditions removing the critical points on the smallest scales, which also correspond to the highest curvature environments where quantum pressure would be the strongest.

The behaviour of the PDFs we see on these scales is quite different to those found in [Dome et al. \(2023\)](#) in the context of classical FDM, where they find peaks to have the most stable PDF across changing cosmologies, and their voids have the most sensitivity to changing cosmology. However this is not immediately surprising as their PDFs are extracted on much smaller scales (0.04 vs 1 Mpc/ h), and their environments are quantified differently (for example, their void PDFs quantify all the matter in the void, while ours consider the PDF of densities at the void-type critical points, roughly the density at the centre of voids). While the behaviour between different environments is quite different, the overall effect of shifting all PDFs towards more overdense values is seen in both cases.

We note as well that in the fully non-linear case, the PDF of peak type critical points is likely to look different on small scales, as in [Dome et al. \(2023\)](#), as a consequence of virialisation creating stable halo profiles which feed into the peak PDF. Since our work considers 1PPT, equivalent to the Zel’dovich approximation in the $\hbar_{\text{PPT}} \rightarrow 0$ limit, our model will not produce virialised objects due to overshooting, and thus we do not see the stability of the peak PDF discussed in [Dome et al. \(2023\)](#).

5. CONCLUSIONS

Summary. In this paper we present an analysis of density fields produced by two perturbative forward models on scales currently inaccessible to full Schrödinger-Poisson solvers. The models considered encode either classical fluid dynamics (LPT) or wave dynamics (PPT). Both dynamics were applied to both CDM and FDM initial conditions to disentangle effects of initial conditions from dynamical interference effects. We demonstrate that the wave-perturbation scheme used provides similar effects on the power spectrum to fully non-linear Schrödinger-Poisson simulations.

For statistics of density environments such as the matter PDF or the reduced skewness S_3 on mildly non-linear scales, we show that the principle difference between fully classical (LPT + CDM ICs) and fully wave (PPT + FDM ICs) dark matter is driven mostly by the suppression of the initial conditions. This gives credibility to the “classical fuzzy dark matter” ([Dome et al. 2023](#)) approach on large perturbative scales for these sorts of averaged cell statistics.

Analysis of the critical points of the density field show that these density field extrema are more sensitive to interference and quantum pressure effects than averaged one-point statistics. This is expected as both the quantum potential and these extrema are sensitive to deriva-

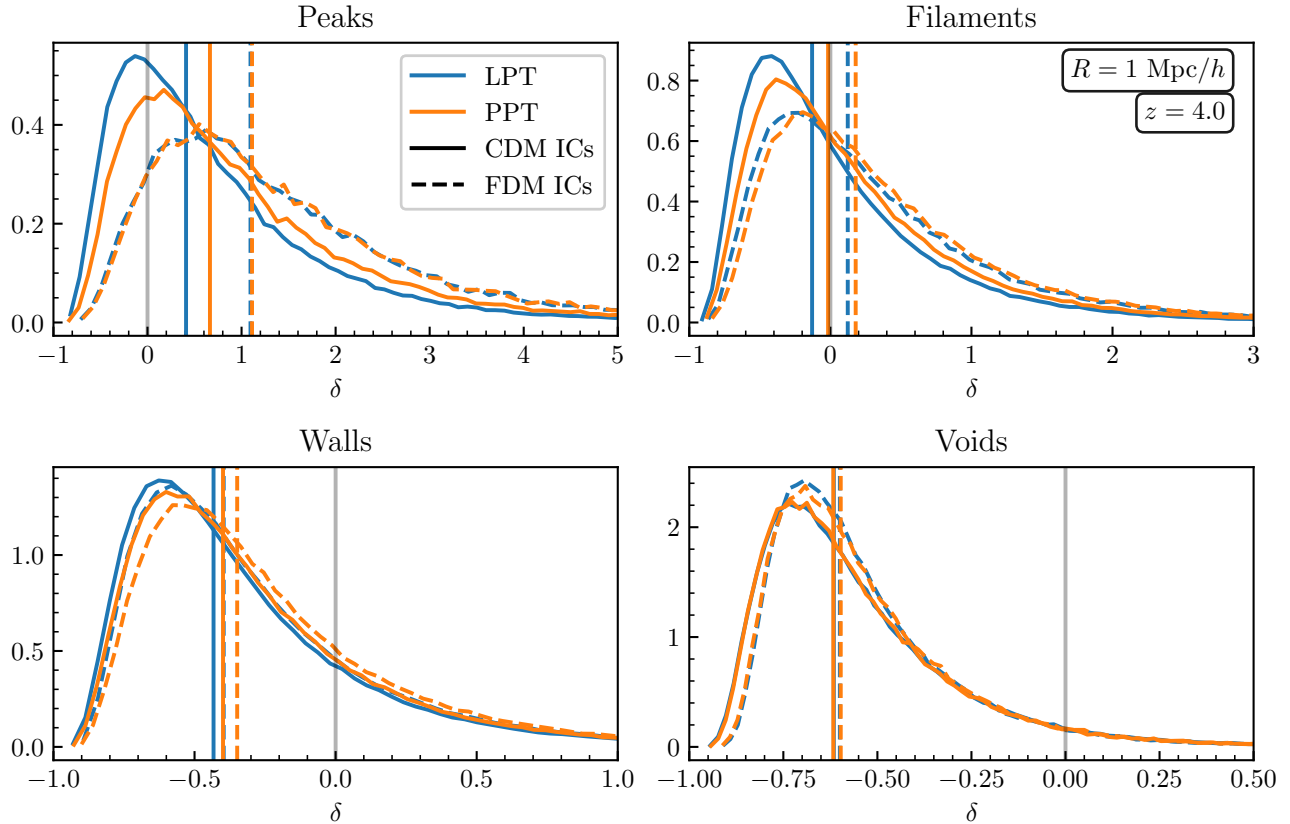


Figure 12. The PDFs of the density found in different critical point environments, linearly interpolated between bins. The vertical lines show the median value of δ for that cosmology, the grey vertical line divides under- and over-dense environments. Environments with more shell crossing, such as peaks, have a larger shift when wave dynamics are turned on, due to the quantum potential having a larger effect.

tives of the underlying density field. Both suppression of the initial power and wave interference affect the total number and relative fraction of critical points, decreasing the amount of gravitational collapse and shell crossing, preferentially erasing critical points which require more shell crossing (peaks and filaments) compared to under-dense type critical points (voids and walls). The one-point statistics of these different critical point environments also clearly demonstrate the role of the quantum pressure, with more collapsed regions producing a larger shift in the PDF compared to the fully classical case.

Outlook. Our analysis suggests that the one-point PDF and skewness of the density field appear fairly insensitive to the presence of wave dynamics on mildly non-linear scales. The prospect for theoretically modelling such statistics in fully non-linear FDM cosmologies is therefore encouraging, requiring only changes to the linear power spectrum. The large-deviations theory model of the matter PDF (Bernardeau et al. 2014; Uhlemann et al. 2016) has successfully been adapted to non- Λ CDM cosmologies (Uhlemann et al. 2020; Cataneo et al. 2022). Because of the promise of the PDF as a non-Gaussian probe of extended cosmologies, a similar forecast or inference based on the matter PDF and related quantities could be a powerful complement to existing statistics in detecting wavelike dark matter effects. Successful modelling of the dark matter PDF in FDM cosmologies could

then be extended to observables such as biased tracers (Uhlemann et al. 2018b; Friedrich et al. 2022) or weak lensing statistics (Reimberg & Bernardeau 2018; Uhlemann et al. 2018a; Barthelemy et al. 2020, 2021, 2022, 2024; Boyle et al. 2023), as has been done in Λ CDM cosmologies.

A variety of other statistics beyond those presented in this work could be extracted from this map-based forward model, further pushing the question of whether the quantum potential imprints signatures on any large scale statistics which are not captured by suppressing the initial conditions. Statistics related to the velocity and velocity dispersion could be extracted by utilising the phase information of the PPT wavefunction. Spatial correlations of/between the critical points of the density field could provide additional information to simple number counts and one-point statistics presented here. Additionally, analysing the sensitivity of different cosmic web identification methods would be a natural extension to this work and could provide insights into the structure of the cosmic web in fuzzy cosmologies.

Our wave-mechanical models present an appealing complementary approach to large scale studies of fuzzy dark matter. With further theoretical work to establish a mapping between \hbar_{PPT} and the FDM particle mass m , propagator perturbation theory could be used as a less numerically intensive method of generating simula-

tions of wave dark matter on large scales. While current hybrid approaches patch large scale N -body with small scale Schrödinger-Poisson solvers, it could be possible to patch this wave based perturbation theory on large scales with Schrödinger-Poisson on small scales, in a similar spirit to COLA (Tassev et al. 2013) and Hi-COLA (Wright et al. 2023). Large scale simulations of wave dark matter which maintain interference effects on all scales would be an important tool for testing if the fundamental nature of dark matter is particle-like or wave-like and derive constraints from astrophysical data.

ACKNOWLEDGEMENTS

We thank the anonymous referees for valuable suggestions that improved the presentation of our results. We thank Oliver Hahn, Cornelius Rampf, and Mateja Gosenca for useful conversations and feedback at multiple stages of this project. AG thanks Alexandre Barthelemy and Oliver Friedrich for discussions with initialised some of this project's ideas. We thank Simon May for discussions and sharing the power spectra data.

The figures in this work were created with MATPLOTLIB (Hunter et al. 2007) making use of the NUMPY (Harris et al. 2020), SCIPY (Virtanen et al. 2020), and SCIKIT-IMAGE (van der Walt et al. 2014) Python libraries.

AG was supported by an EPSRC studentship under Project 2441314 from UK Research & Innovation. CU's research was supported in part by grant NSF PHY-1748958 to the Kavli Institute for Theoretical Physics (KITP) and in part funded by the European Union (ERC StG, LSS_BeyondAverage, 101075919). AG and CU are grateful for the hospitality of Perimeter Institute where this work was finalised following peer review. Research at Perimeter Institute is supported in part by the Government of Canada through the Department of Innovation, Science and Economic Development and by the Province of Ontario through the Ministry of Colleges and Universities. This research was also supported in part by the Simons Foundation through the Simons Foundation Emmy Noether Fellows Program at Perimeter Institute.

DATA ACCESS STATEMENT

The data in this paper was created using publicly available codes, using input parameters detailed in the body of the text. For the purpose of open access, the authors have applied a 'Creative Commons Attribution' (CC BY) licence to this paper.

REFERENCES

- Almgren, A. S., Bell, J. B., Lijewski, M. J., Lukić, Z., & Van Andel, E. 2013, *The Astrophysical Journal*, 765, 39, doi: [10.1088/0004-637X/765/1/39](https://doi.org/10.1088/0004-637X/765/1/39)
- Aragón-Calvo, M. A., Platen, E., van de Weygaert, R., & Szalay, A. S. 2010, *The Astrophysical Journal*, 723, 364, doi: [10.1088/0004-637X/723/1/364](https://doi.org/10.1088/0004-637X/723/1/364)
- Armengaud, E., Palanque-Delabrouille, N., Yèche, C., Marsh, D. J. E., & Baur, J. 2017, *MNRAS*, 471, 4606, doi: [10.1093/mnras/stx1870](https://doi.org/10.1093/mnras/stx1870)
- Arvanitaki, A., Dimopoulos, S., Dubovsky, S., Kaloper, N., & March-Russell, J. 2010, *Phys. Rev. D*, 81, 123530, doi: [10.1103/PhysRevD.81.123530](https://doi.org/10.1103/PhysRevD.81.123530)
- Aycoberly, E., Barthelemy, A., & Codis, S. 2023, A Theoretical View on the T-web Statistical Description of the Cosmic Web, doi: [10.48550/arXiv.2310.03548](https://doi.org/10.48550/arXiv.2310.03548)
- Bardeen, J. M., Bond, J. R., Kaiser, N., & Szalay, A. S. 1986, *The Astrophysical Journal*, 304, 15, doi: [10.1086/164143](https://doi.org/10.1086/164143)
- Barthelemy, A., Bernardeau, F., Codis, S., & Uhlemann, C. 2022, *Phys. Rev. D*, 105, doi: [10.1103/PhysRevD.105.043537](https://doi.org/10.1103/PhysRevD.105.043537)
- Barthelemy, A., Codis, S., & Bernardeau, F. 2021, *MNRAS*, 503, 5204, doi: [10.1093/mnras/stab818](https://doi.org/10.1093/mnras/stab818)
- Barthelemy, A., Codis, S., Uhlemann, C., Bernardeau, F., & Gavazzi, R. 2020, *MNRAS*, 492, 3420, doi: [10.1093/mnras/staa053](https://doi.org/10.1093/mnras/staa053)
- Barthelemy, A., Halder, A., Gong, Z., & Uhlemann, C. 2024, *J. Cosmology Astropart. Phys.*, 2024, 060, doi: [10.1088/1475-7516/2024/03/060](https://doi.org/10.1088/1475-7516/2024/03/060)
- Bernardeau, F. 1994a, *The Astrophysical Journal*, 433, 1, doi: [10.1086/174620](https://doi.org/10.1086/174620)
- . 1994b, *Astronomy and Astrophysics*, 291, 697, doi: [10.48550/arXiv.astro-ph/9403020](https://doi.org/10.48550/arXiv.astro-ph/9403020)
- Bernardeau, F., Colombi, S., Gaztañaga, E., & Scoccimarro, R. 2002, *Phys. Rep.*, 367, 1, doi: [10.1016/S0370-1573\(02\)00135-7](https://doi.org/10.1016/S0370-1573(02)00135-7)
- Bernardeau, F., & Kofman, L. 1995, *ApJ*, 443, 479, doi: [10.1086/175542](https://doi.org/10.1086/175542)
- Bernardeau, F., Pichon, C., & Codis, S. 2014, *Phys. Rev. D*, 90, 103519, doi: [10.1103/PhysRevD.90.103519](https://doi.org/10.1103/PhysRevD.90.103519)
- Boyle, A., Barthelemy, A., Codis, S., et al. 2023, *The Open Journal of Astrophysics*, 6, 22, doi: [10.21105/astro.2212.10351](https://doi.org/10.21105/astro.2212.10351)
- Brenier, Y., Frisch, U., Hénon, M., et al. 2003, *MNRAS*, 346, 501, doi: [10.1046/j.1365-2966.2003.07106.x](https://doi.org/10.1046/j.1365-2966.2003.07106.x)
- Bull, P., Akrami, Y., Adamek, J., et al. 2016, *Physics of the Dark Universe*, 12, 56, doi: [10.1016/j.dark.2016.02.001](https://doi.org/10.1016/j.dark.2016.02.001)
- Carlesi, E., Knebe, A., Lewis, G. F., Wales, S., & Yepes, G. 2014, *Monthly Notices of the Royal Astronomical Society*, 439, 2943, doi: [10.1093/mnras/stu150](https://doi.org/10.1093/mnras/stu150)
- Cataneo, M., Uhlemann, C., Arnold, C., et al. 2022, *Monthly Notices of the Royal Astronomical Society*, 513, 1623, doi: [10.1093/mnras/stac904](https://doi.org/10.1093/mnras/stac904)
- Cautun, M., van de Weygaert, R., & Jones, B. J. T. 2013, *Monthly Notices of the Royal Astronomical Society*, 429, 1286, doi: [10.1093/mnras/sts416](https://doi.org/10.1093/mnras/sts416)
- Chavanis, P. H. 2012, *Astronomy and Astrophysics*, 537, A127, doi: [10.1051/0004-6361/201116905](https://doi.org/10.1051/0004-6361/201116905)
- Coles, P., & Spencer, K. 2003, *MNRAS*, 342, 176, doi: [10.1046/j.1365-8711.2003.06529.x](https://doi.org/10.1046/j.1365-8711.2003.06529.x)
- Colombi, S., Pogosyan, D., & Souradeep, T. 2000, *Physical Review Letters*, 85, 5515, doi: [10.1103/PhysRevLett.85.5515](https://doi.org/10.1103/PhysRevLett.85.5515)
- Cui, W., Knebe, A., Yepes, G., et al. 2018, *Monthly Notices of the Royal Astronomical Society*, 473, 68, doi: [10.1093/mnras/stx2323](https://doi.org/10.1093/mnras/stx2323)
- Dalal, N., & Kravtsov, A. 2022, *Phys. Rev. D*, 106, 063517, doi: [10.1103/PhysRevD.106.063517](https://doi.org/10.1103/PhysRevD.106.063517)
- Desjacques, V., Kehagias, A., & Riotto, A. 2018, *Phys. Rev. D*, 97, 023529, doi: [10.1103/PhysRevD.97.023529](https://doi.org/10.1103/PhysRevD.97.023529)
- Di Valentino, E., Anchordoqui, L. A., Akarsu, Ö., et al. 2021, *Astroparticle Physics*, 131, 102604, doi: [10.1016/j.astropartphys.2021.102604](https://doi.org/10.1016/j.astropartphys.2021.102604)
- Dome, T., Fialkov, A., Mocz, P., et al. 2023, *Monthly Notices of the Royal Astronomical Society*, 519, 4183, doi: [10.1093/mnras/stac3766](https://doi.org/10.1093/mnras/stac3766)
- Dome, T., Fialkov, A., Sartorio, N., & Mocz, P. 2023, *MNRAS*, 525, 348, doi: [10.1093/mnras/stad2276](https://doi.org/10.1093/mnras/stad2276)
- Douspis, M., Salvati, L., & Aghanim, N. 2019, arXiv e-prints. <https://arxiv.org/abs/1901.05289>
- Edwards, F., Kendall, E., Hotchkiss, S., & Easther, R. 2018, *Journal of Cosmology and Astroparticle Physics*, 2018, 027, doi: [10.1088/1475-7516/2018/10/027](https://doi.org/10.1088/1475-7516/2018/10/027)
- Falck, B. L., Neyrinck, M. C., & Szalay, A. S. 2012, *The Astrophysical Journal*, 754, 126, doi: [10.1088/0004-637X/754/2/126](https://doi.org/10.1088/0004-637X/754/2/126)
- Ferreira, E. G. M. 2021, *A&A Rev.*, 29, 7, doi: [10.1007/s00159-021-00135-6](https://doi.org/10.1007/s00159-021-00135-6)
- Forero-Romero, J. E., Hoffman, Y., Gottlöber, S., Klypin, A., & Yepes, G. 2009, *Monthly Notices of the Royal Astronomical Society*, 396, 1815, doi: [10.1111/j.1365-2966.2009.14885.x](https://doi.org/10.1111/j.1365-2966.2009.14885.x)
- Frenk, C. S., & White, S. D. M. 2012, *Annalen der Physik*, 524, 507, doi: [10.1002/andp.201200212](https://doi.org/10.1002/andp.201200212)
- Friedrich, O., Halder, A., Boyle, A., et al. 2022, *MNRAS*, 510, 5069, doi: [10.1093/mnras/stab3703](https://doi.org/10.1093/mnras/stab3703)
- Gallagher, A., & Coles, P. 2022, *The Open Journal of Astrophysics*, 5, 17, doi: [10.21105/astro.2208.13851](https://doi.org/10.21105/astro.2208.13851)
- Gay, C., Pichon, C., & Pogosyan, D. 2012, *Physical Review D*, 85, 023011, doi: [10.1103/PhysRevD.85.023011](https://doi.org/10.1103/PhysRevD.85.023011)
- Glennon, N., Musoke, N., & Prescod-Weinstein, C. 2023, *Physical Review D*, 107, 063520, doi: [10.1103/PhysRevD.107.063520](https://doi.org/10.1103/PhysRevD.107.063520)
- Gosenca, M., Eberhardt, A., Wang, Y., et al. 2023, *Phys. Rev. D*, 107, 083014, doi: [10.1103/PhysRevD.107.083014](https://doi.org/10.1103/PhysRevD.107.083014)
- Gough, A., & Uhlemann, C. 2022, *The Open Journal of Astrophysics*, 5, 14, doi: [10.21105/astro.2206.11918](https://doi.org/10.21105/astro.2206.11918)
- Guo, H.-K., Sinha, K., Sun, C., Swaim, J., & Vagie, D. 2021, *J. Cosmology Astropart. Phys.*, 2021, 028, doi: [10.1088/1475-7516/2021/10/028](https://doi.org/10.1088/1475-7516/2021/10/028)
- Guth, A. H., Hertzberg, M. P., & Prescod-Weinstein, C. 2015, 92, 103513, doi: [10.1103/PhysRevD.92.103513](https://doi.org/10.1103/PhysRevD.92.103513)

- Hahn, O., Rampf, C., & Uhlemann, C. 2021, MNRAS, 503, 426, doi: [10.1093/mnras/staa3773](https://doi.org/10.1093/mnras/staa3773)
- Harris et al., C. R. 2020, Nature, 585, 357, doi: [10.1038/s41586-020-2649-2](https://doi.org/10.1038/s41586-020-2649-2)
- Hložek, R., Marsh, D. J. E., & Grin, D. 2018, MNRAS, 476, 3063, doi: [10.1093/mnras/sty271](https://doi.org/10.1093/mnras/sty271)
- Hložek, R., Grin, D., Marsh, D. J. E., & Ferreira, P. G. 2015, Physical Review D, 91, 103512, doi: [10.1103/PhysRevD.91.103512](https://doi.org/10.1103/PhysRevD.91.103512)
- Hoffman, Y., Metuki, O., Yepes, G., et al. 2012, Monthly Notices of the Royal Astronomical Society, 425, 2049, doi: [10.1111/j.1365-2966.2012.21553.x](https://doi.org/10.1111/j.1365-2966.2012.21553.x)
- Hopkins, P. F. 2019, MNRAS, 489, 2367, doi: [10.1093/mnras/stz1922](https://doi.org/10.1093/mnras/stz1922)
- Hu, W., Barkana, R., & Gruzinov, A. 2000, Physical Review Letters, 85, 1158, doi: [10.1103/PhysRevLett.85.1158](https://doi.org/10.1103/PhysRevLett.85.1158)
- Huang, H., Schive, H.-Y., & Chiueh, T. 2023, MNRAS, 522, 515, doi: [10.1093/mnras/stad998](https://doi.org/10.1093/mnras/stad998)
- Hui, L. 2021, ARA&A, 59, doi: [10.1146/annurev-astro-120920-010024](https://doi.org/10.1146/annurev-astro-120920-010024)
- Hui, L., Ostriker, J. P., Tremaine, S., & Witten, E. 2017, Phys. Rev. D, 95, 043541, doi: [10.1103/PhysRevD.95.043541](https://doi.org/10.1103/PhysRevD.95.043541)
- Hunter et al., J. D. 2007, Computing in Science & Engineering, 9, 90, doi: [10.1109/MCSE.2007.55](https://doi.org/10.1109/MCSE.2007.55)
- Iršič, V., Viel, M., Haehnelt, M. G., Bolton, J. S., & Becker, G. D. 2017, Phys. Rev. Lett., 119, 031302, doi: [10.1103/PhysRevLett.119.031302](https://doi.org/10.1103/PhysRevLett.119.031302)
- Ivezić, Ž., Kahn, S. M., & Tyson et al., J. A. 2019, ApJ, 873, 111, doi: [10.3847/1538-4357/ab042c](https://doi.org/10.3847/1538-4357/ab042c)
- Jaekel, J., Rybka, G., & Winslow, L. 2022, arXiv e-prints. <https://arxiv.org/abs/2203.14923>
- Kobayashi, T., Murgia, R., De Simone, A., Iršič, V., & Viel, M. 2017, Phys. Rev. D, 96, 123514, doi: [10.1103/PhysRevD.96.123514](https://doi.org/10.1103/PhysRevD.96.123514)
- Laguë, A., Bond, J. R., Hložek, R., Marsh, D. J. E., & Söding, L. 2021, MNRAS, 504, 2391, doi: [10.1093/mnras/stab601](https://doi.org/10.1093/mnras/stab601)
- Laguë, A., Schwabe, B., Hložek, R., Marsh, D. J. E., & Rogers, K. K. 2024, Phys. Rev. D, 109, 043507, doi: [10.1103/PhysRevD.109.043507](https://doi.org/10.1103/PhysRevD.109.043507)
- Laureijs et al., R. 2011, arXiv e-prints. <https://arxiv.org/abs/1110.3193>
- Leong, K.-H., Schive, H.-Y., Zhang, U.-H., & Chiueh, T. 2019, MNRAS, 484, 4273, doi: [10.1093/mnras/stz271](https://doi.org/10.1093/mnras/stz271)
- Levi et al., M. 2013, arXiv e-prints, arXiv:1308.0847. <https://arxiv.org/abs/1308.0847>
- Lewis, A., & Bridle, S. 2002, Physical Review D, 66, 103511, doi: [10.1103/PhysRevD.66.103511](https://doi.org/10.1103/PhysRevD.66.103511)
- Li, X., Hui, L., & Bryan, G. L. 2019, Physical Review D, 99, 063509, doi: [10.1103/PhysRevD.99.063509](https://doi.org/10.1103/PhysRevD.99.063509)
- Libeskind, N. I., van de Weygaert, R., Cautun, M., et al. 2018, Monthly Notices of the Royal Astronomical Society, 473, 1195, doi: [10.1093/mnras/stx1976](https://doi.org/10.1093/mnras/stx1976)
- Luu, H. N., Mocz, P., Vogelsberger, M., et al. 2024, MNRAS, 527, 4162, doi: [10.1093/mnras/stad3482](https://doi.org/10.1093/mnras/stad3482)
- Madelung, E. 1927, Zeitschrift für Physik, 40, 322, doi: [10.1007/BF01400372](https://doi.org/10.1007/BF01400372)
- Manouchehri Kousha, H., Hooshangi, S., & Abolhasani, A. 2024, The Astrophysical Journal, 961, 131, doi: [10.3847/1538-4357/ad148f](https://doi.org/10.3847/1538-4357/ad148f)
- Marsh, D. J. E. 2015, Physical Review D, 91, 123520, doi: [10.1103/PhysRevD.91.123520](https://doi.org/10.1103/PhysRevD.91.123520)
- . 2016, Physics Reports, 643, 1, doi: [10.1016/j.physrep.2016.06.005](https://doi.org/10.1016/j.physrep.2016.06.005)
- May, S., & Springel, V. 2021, MNRAS, 506, 2603, doi: [10.1093/mnras/stab1764](https://doi.org/10.1093/mnras/stab1764)
- May, S., & Springel, V. 2023, Monthly Notices of the Royal Astronomical Society, 524, 4256, doi: [10.1093/mnras/stad2031](https://doi.org/10.1093/mnras/stad2031)
- Melott, A. L., Pellman, T. F., & Shandarin, S. F. 1994, MNRAS, 269, 626, doi: [10.1093/mnras/269.3.626](https://doi.org/10.1093/mnras/269.3.626)
- Michaux, M., Hahn, O., Rampf, C., & Angulo, R. E. 2021, Monthly Notices of the Royal Astronomical Society, 500, 663, doi: [10.1093/mnras/staa3149](https://doi.org/10.1093/mnras/staa3149)
- Mocz, P., & Succi, S. 2015, Phys. Rev. E, 91, 053304, doi: [10.1103/PhysRevE.91.053304](https://doi.org/10.1103/PhysRevE.91.053304)
- Mocz, P., Fialkov, A., Vogelsberger, M., et al. 2019, Phys. Rev. Lett., 123, 141301, doi: [10.1103/PhysRevLett.123.141301](https://doi.org/10.1103/PhysRevLett.123.141301)
- Mocz, P., Fialkov, A., Vogelsberger, M., et al. 2023, MNRAS, 521, 2608, doi: [10.1093/mnras/stad694](https://doi.org/10.1093/mnras/stad694)
- Munshi, D., Sahni, V., & Starobinsky, A. A. 1994, The Astrophysical Journal, 436, 517, doi: [10.1086/174925](https://doi.org/10.1086/174925)
- Nori, M., & Baldi, M. 2018, MNRAS, 478, 3935, doi: [10.1093/mnras/sty1224](https://doi.org/10.1093/mnras/sty1224)
- O'Hare, C. 2020, cajohare/AxionLimits: AxionLimits, v1.0, <https://cajohare.github.io/AxionLimits/>, Zenodo, doi: [10.5281/zenodo.3932430](https://doi.org/10.5281/zenodo.3932430)
- O'Hare, C. A. J. 2024, arXiv e-prints, arXiv:2403.17697, doi: [10.48550/arXiv.2403.17697](https://doi.org/10.48550/arXiv.2403.17697)
- Painter, C. A., Boylan-Kolchin, M., Mocz, P., & Vogelsberger, M. 2024, An attractive model: simulating fuzzy dark matter with attractive self-interactions. <https://arxiv.org/abs/2402.16945>
- Peccei, R. D., & Quinn, H. R. 1977, Phys. Rev. Lett., 38, 1440, doi: [10.1103/PhysRevLett.38.1440](https://doi.org/10.1103/PhysRevLett.38.1440)
- Perivolaropoulos, L., & Skara, F. 2022, New A Rev., 95, 101659, doi: [10.1016/j.newar.2022.101659](https://doi.org/10.1016/j.newar.2022.101659)
- Planck Collaboration, Aghanim, N., Akrami, Y., et al. 2020, A&A, 641, A1, doi: [10.1051/0004-6361/201833880](https://doi.org/10.1051/0004-6361/201833880)
- Porqueres, N., Hahn, O., Jasche, J., & Lavaux, G. 2020, Astronomy & Astrophysics, 642, A139, doi: [10.1051/0004-6361/202038482](https://doi.org/10.1051/0004-6361/202038482)
- Rampf, C., Uhlemann, C., & Hahn, O. 2021, MNRAS, 503, 406, doi: [10.1093/mnras/staa3605](https://doi.org/10.1093/mnras/staa3605)
- Reimberg, P., & Bernardeau, F. 2018, Phys. Rev. D, 97, 023524, doi: [10.1103/PhysRevD.97.023524](https://doi.org/10.1103/PhysRevD.97.023524)
- Rogers, K. K., Dvorkin, C., & Peiris, H. V. 2022, Phys. Rev. Lett., 128, 171301, doi: [10.1103/PhysRevLett.128.171301](https://doi.org/10.1103/PhysRevLett.128.171301)
- Rogers, K. K., Hložek, R., Laguë, A., et al. 2023, J. Cosmology Astropart. Phys., 2023, 023, doi: [10.1088/1475-7516/2023/06/023](https://doi.org/10.1088/1475-7516/2023/06/023)
- Schive, H.-Y., Chiueh, T., & Broadhurst, T. 2014, Nature Physics, 10, 496, doi: [10.1038/nphys2996](https://doi.org/10.1038/nphys2996)
- Schwabe, B., Gosenca, M., Behrens, C., Niemeyer, J. C., & Easther, R. 2020, Physical Review D, 102, 083518, doi: [10.1103/PhysRevD.102.083518](https://doi.org/10.1103/PhysRevD.102.083518)
- Schwabe, B., & Niemeyer, J. C. 2022, Phys. Rev. Lett., 128, 181301, doi: [10.1103/PhysRevLett.128.181301](https://doi.org/10.1103/PhysRevLett.128.181301)
- Soccimarro, R., & Frieman, J. 1996, 105, 37, doi: [10.1086/192306](https://doi.org/10.1086/192306)
- Shim, J., Codis, S., Pichon, C., Pogosyan, D., & Cadiou, C. 2021, Monthly Notices of the Royal Astronomical Society, 502, 3885, doi: [10.1093/mnras/stab263](https://doi.org/10.1093/mnras/stab263)
- Short, C. J., & Coles, P. 2006, J. Cosmology Astropart. Phys., 2006, 016, doi: [10.1088/1475-7516/2006/12/016](https://doi.org/10.1088/1475-7516/2006/12/016)
- Sousbie, T. 2011, Monthly Notices of the Royal Astronomical Society, 414, 350, doi: [10.1111/j.1365-2966.2011.18394.x](https://doi.org/10.1111/j.1365-2966.2011.18394.x)
- Sousbie, T., Pichon, C., & Kawahara, H. 2011, Monthly Notices of the Royal Astronomical Society, 414, 384, doi: [10.1111/j.1365-2966.2011.18395.x](https://doi.org/10.1111/j.1365-2966.2011.18395.x)
- Springel, V. 2005, Monthly Notices of the Royal Astronomical Society, 364, 1105, doi: [10.1111/j.1365-2966.2005.09655.x](https://doi.org/10.1111/j.1365-2966.2005.09655.x)
- Suárez-Pérez, J. F., Camargo, Y., Li, X.-D., & Forero-Romero, J. E. 2021, The Astrophysical Journal, 922, 204, doi: [10.3847/1538-4357/ac1fed](https://doi.org/10.3847/1538-4357/ac1fed)
- Svrcek, P., & Witten, E. 2006, Journal of High Energy Physics, 2006, 051, doi: [10.1088/1126-6708/2006/06/051](https://doi.org/10.1088/1126-6708/2006/06/051)
- Tassev, S., Zaldarriaga, M., & Eisenstein, D. J. 2013, Journal of Cosmology and Astroparticle Physics, 2013, 036, doi: [10.1088/1475-7516/2013/06/036](https://doi.org/10.1088/1475-7516/2013/06/036)
- Uhlemann, C., Codis, S., Pichon, C., Bernardeau, F., & Reimberg, P. 2016, MNRAS, 460, 1529, doi: [10.1093/mnras/stw1074](https://doi.org/10.1093/mnras/stw1074)
- Uhlemann, C., Friedrich, O., Villaescusa-Navarro, F., Banerjee, A., & Codis, S. 2020, MNRAS, 495, 4006, doi: [10.1093/mnras/staa1155](https://doi.org/10.1093/mnras/staa1155)
- Uhlemann, C., Kopp, M., & Haug, T. 2014, Phys. Rev. D, 90, 023517, doi: [10.1103/PhysRevD.90.023517](https://doi.org/10.1103/PhysRevD.90.023517)
- Uhlemann, C., Pichon, C., Codis, S., et al. 2018a, MNRAS, 477, 2772, doi: [10.1093/mnras/sty664](https://doi.org/10.1093/mnras/sty664)
- Uhlemann, C., Rampf, C., Gosenca, M., & Hahn, O. 2019, Physical Review D, 99, doi: [10.1103/physrevd.99.083524](https://doi.org/10.1103/physrevd.99.083524)
- Uhlemann, C., Feix, M., Codis, S., et al. 2018b, MNRAS, 473, 5098, doi: [10.1093/mnras/stx2616](https://doi.org/10.1093/mnras/stx2616)
- van der Walt et al., S. 2014, PeerJ, 2, e453, doi: [10.7717/peerj.453](https://doi.org/10.7717/peerj.453)
- Veltmaat, J., & Niemeyer, J. C. 2016, Phys. Rev. D, 94, 123523, doi: [10.1103/PhysRevD.94.123523](https://doi.org/10.1103/PhysRevD.94.123523)
- Villaescusa-Navarro, F. 2018, Pylians: Python libraries for the analysis of numerical simulations, Astrophysics Source Code Library, record ascl:1811.008. <http://ascl.net/1811.008>
- Virtanen et al., P. 2020, Nature Methods, 17, 261, doi: [10.1038/s41592-019-0686-2](https://doi.org/10.1038/s41592-019-0686-2)
- Widrow, L. M., & Kaiser, N. 1993, ApJL, 416, L71, doi: [10.1086/187073](https://doi.org/10.1086/187073)
- Winch, H., Rogers, K. K., Hložek, R., & Marsh, D. J. E. 2024, arXiv e-prints, arXiv:2404.11071, doi: [10.48550/arXiv.2404.11071](https://doi.org/10.48550/arXiv.2404.11071)
- Wright, B. S., Sen Gupta, A., Baker, T., et al. 2023, Journal of Cosmology and Astroparticle Physics, 2023, 040, doi: [10.1088/1475-7516/2023/03/040](https://doi.org/10.1088/1475-7516/2023/03/040)
- Zel'dovich, Y. B. 1970, A&A, 5, 84
- Zhang, J., Kuo, J.-L., Liu, H., et al. 2018, The Astrophysical Journal, 863, 73, doi: [10.3847/1538-4357/aac3f3](https://doi.org/10.3847/1538-4357/aac3f3)

APPENDIX

A. MATCHING PPT SCALE AND FDM MASS

A.1. Effect of larger \hbar_{PPT}

Figures 13 and 14 show the power spectrum and reduced skewness as in Figures 2 and 5, now with an additional values of \hbar_{PPT} . A value of $\hbar_{\text{PPT}} = 2.2 h^{-2} \text{ Mpc}^2$ (twice the value used in the main analysis) produces skewness enhancements similar to those due to changing the initial conditions through wave dynamics alone (compare the red/triangle solid line to the blue/circle or orange/square dashed lines). The choice of $\hbar_{\text{PPT}} = 6 h^{-2} \text{ Mpc}^2$ leads to a suppression in the power spectrum similar to the linearly evolved FDM power spectrum for $m_{22} = 0.1$. Since full Schrödinger-Poisson simulations indicate that these scales should see power exceeding the linearly predicted value (see Figure 3) this suggests that this choice of \hbar_{PPT} is not well matched to the mass used to set the initial conditions $m_{22} = 0.1$. Based on this we do not expect $m_{22} = 0.1$ to map to an \hbar_{PPT} greater than $6 h^{-2} \text{ Mpc}^2$. In this sense, our choice of $\hbar_{\text{PPT}} = 1.1 h^{-2} \text{ Mpc}^2$ provides a conservative estimate of the effect of wave dynamics compared to initial conditions. It may be possible to determine a more precise mapping between \hbar_{PPT} and m_{22} for which ideas are sketched in Appendix A.3.

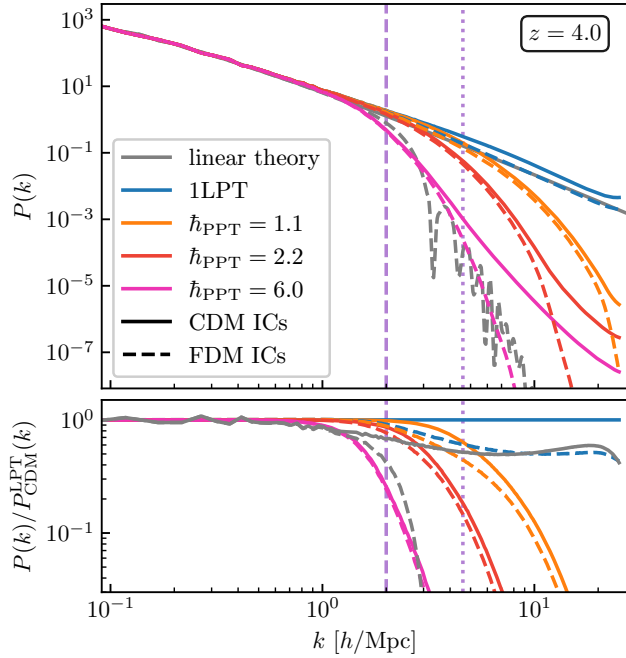


Figure 13. Same as Figure 2 with two additional values of \hbar_{PPT} . The power spectrum with $\hbar_{\text{PPT}} = 6 h^{-2} \text{ Mpc}^2$ sees comparable suppression to the linear FDM power spectrum (grey dashed) at $z = 4$. Full Schrödinger-Poisson simulations indicate these scales should have been enhanced by non-linear evolution by redshift 4, indicating that $\hbar_{\text{PPT}} = 6 h^{-2} \text{ Mpc}^2$ is not well matched to the mass $m_{22} = 0.1$.

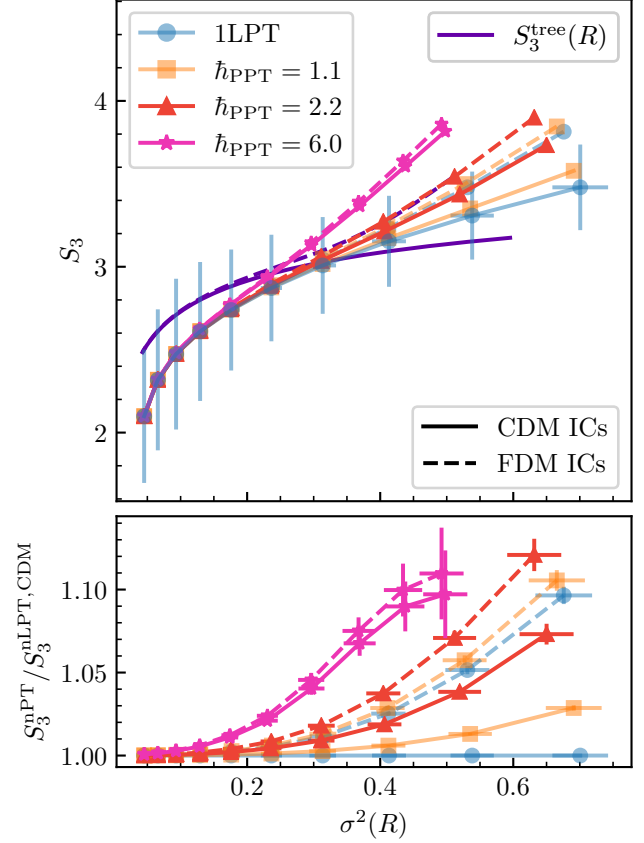


Figure 14. Same as Figure 5 with the additional values \hbar_{PPT} . The larger value of the LPT + FDM ICs case even on cold initial conditions. The $\hbar_{\text{PPT}} = 6 h^{-2} \text{ Mpc}^2$ produces a significantly enhanced S_3 , driven by the dynamics rather than the initial conditions. The lines previously shown are made slightly transparent to aid readability.

A.2. The role of time variables

Here we comment on the difference in coordinates between the PPT wave dynamics and the true FDM style equations (which are the same as the Widrow-Kaiser style application of Schrödinger-Poisson to modelling CDM). This is also discussed in Uhlemann et al. (2019).

The PPT equations take the scale factor a as the time variable, rather than the cosmic time t as in equations (1). This impacts the natural velocity/momentum variable in the two pictures: in PPT it is $\mathbf{v} = d\mathbf{x}/da = \nabla\phi_v$ which differs from the peculiar velocity $\mathbf{u} = d\mathbf{x}/dt = \dot{a}\mathbf{v} = H_0 a^2 \mathbf{v}$ which is generated by the wavefunction phase in the FDM scenario (5b). This leads to the identification $\phi = \dot{a} a^2 \phi_v$ as the mapping between the phase in the FDM picture and the PPT picture. These variable changes amount to a non-canonical transformation in phase space, and are what lead to the differing powers of a in the quantum potentials in the two formulations. Specialising to an Einstein-de Sitter universe, where $\dot{a} \stackrel{\text{EdS}}{=} H_0 a^{-1/2}$ and $\Omega_m^0 = 1$, the relationship between these wavefunction phases is $\phi \stackrel{\text{EdS}}{=} H_0 a^{3/2} \phi_v$.

Rewriting the fluid equation (5) for FDM in a -time,

we can make more direct comparison between these systems. The continuity equation becomes the same as that in PPT (12a), under the mapping between phase variables. Defining the rescaled the gravitational potential by $\varphi_g \stackrel{\text{EdS}}{=} 2V_N/(3H_0^2)$, the FDM Poisson equation (5c) becomes the PPT Poisson equation (12c). The Bernoulli equation (5b) becomes

$$\partial_a \phi_v + \frac{1}{2} |\nabla \phi_v|^2 \stackrel{\text{EdS}}{=} -\frac{3}{2a} (\varphi_g + \phi_v) + \frac{\hbar^2}{2a^3 H_0^2} \frac{\nabla^2 \sqrt{1+\delta}}{\sqrt{1+\delta}}. \quad (\text{A1})$$

Comparing this to the PPT Bernoulli equation (12a) we see that the quantum potential term carries an additional factor of a^3 in EdS spacetimes (more generally a factor of $(\dot{a}a^2)^2$), leaving the \hbar_{PPT} to be interpreted as a time dependent coarse-graining scale, or because the quantum potential in the true FDM case is controlled by the boson mass, \hbar_{PPT} acts like a time dependent mass.

A.3. Mapping \hbar_{PPT} to FDM mass

As the PPT velocity potential ϕ_v generates the velocity $\mathbf{v} = d\mathbf{x}/da$ which has dimensions of length, \hbar_{PPT} must then have dimensions of $[\text{length}]^2$. The mapping between the semiclassical parameter \hbar_{PPT} and the physical FDM particle mass m_{22} isn't straightforwardly 1-to-1 due to the different time evolutions of the quantum potential terms (effectively the \hbar_{PPT} time dependence). Additionally, numerical applications of these systems require different initial conditions, with true FDM requiring initial conditions set by the physical dynamics at some fixed early time, while perturbation theories formally evolve from an initial time of $a \rightarrow 0$ on tethered initial conditions like those discussed in equation (13).

For the purposes of this investigation we take a code-driven approach to choosing \hbar_{PPT} associated with a mass m_{22} , which we discuss in Section 3. Here we outline ideas for an analytic matching which could be implemented in future work.

The naïve approach to matching the FDM particle mass and the \hbar_{PPT} value is to simply equate the strength of the quantum potential terms in equations (A1) and (12b) at some matching redshift z_m . For EdS, this results in

$$\frac{\hbar_{\text{PPT}}}{(\text{Mpc}/h)^2} = \frac{1.34 \times 10^{-4}}{m_{22}} (1+z_m)^{-3/2} \left(\frac{\hbar}{0.7} \right). \quad (\text{A2})$$

If we fix $m_{22} = 0.1$ as the smallest value of FDM particle mass of interest at $z_m = 10$, the resulting $\hbar_{\text{PPT}} \sim 0.05 h^{-2} \text{Mpc}^2$, which is too small to resolve on a reasonably computationally cheap grid scale without aliasing in the wavefunction. When choosing a matching redshift of $z_m = 100$, one gets $\hbar_{\text{PPT}} \sim 1.4 h^{-2} \text{Mpc}^2$, which is close to our choice. However, the matching prescription (A2) is crude as the physical effect of interest is the integrated impact of the quantum potential term on the density field. Neglecting the spatial variation due to density (and $\delta \rightarrow 0$ as $a \rightarrow 0$), the matching cannot be extended all the way to $a_s \rightarrow 0$ as the perturbation theory would require. However, as the quantum potential should only be relevant once enough curvature in the density field is sourced—which will later cause interference in regions of classical shell crossing—this integration should only

be carried back to the onset of structure formation, expected to be relevant from around $z_s = \mathcal{O}(10 - 100)$. If we assumed the Schrödinger-Poisson quantum potential in equation (A1) scales as $Q_{m_{22}}(a)$ compared to a PPT quantum potential in equation (12b) scaling like $Q_{\hbar_{\text{PPT}}}(a)$, matching their integrated effects aggregated over a period from a_s to a_f corresponds to computing a correction factor like

$$f_{\hbar_{\text{PPT}},\text{eff}}(z_s, z_f) \propto \sqrt{\frac{\int_{a_s}^{a_f} da Q_{m_{22}}(a)}{\int_{a_s}^{a_f} da Q_{\hbar_{\text{PPT}}}(a)}}, \quad (\text{A3})$$

where $a = (1+z)^{-1}$. Neglecting the temporal variation of the density, one might assume $Q_{m_{22}}(a) = a^{-3}$ and $Q_{\hbar_{\text{PPT}}}(a) = 1$. This leads to $f_{\hbar_{\text{PPT}},\text{eff}}(4, 10) = 21$ and $f_{\hbar_{\text{PPT}},\text{eff}}(4, 100) = 164$. When considering the leading order temporal evolution of $\delta \propto a$, we would have $Q_{m_{22}} = a^{-2}$ and $Q_{\hbar_{\text{PPT}}}(a) = a$, which leads to values of the same order of magnitude $f_{\hbar_{\text{PPT}},\text{eff}}(4, 10) = 19$ and $f_{\hbar_{\text{PPT}},\text{eff}}(4, 100) = 70$, and hence a similar order of magnitude.

A more precise analysis of what redshift shell crossing becomes sufficiently large to affect this could for example be investigated in a simple one-dimensional comparison between PPT and a full Schrödinger-Poisson solver.

B. IMPACT OF MASS ASSIGNMENT SCHEME

Figure 16 shows the density field constructed from particle positions for 1LPT + FDM ICs using different mass assignment schemes of increasing order. The fine grained pattern, particularly noticeable in the underdense region worsens with lower order mass assignment schemes such as nearest grid point (NGP) and smooths out with higher order schemes such as piecewise cubic spline (PCS). For statistics in the main analysis we anal-

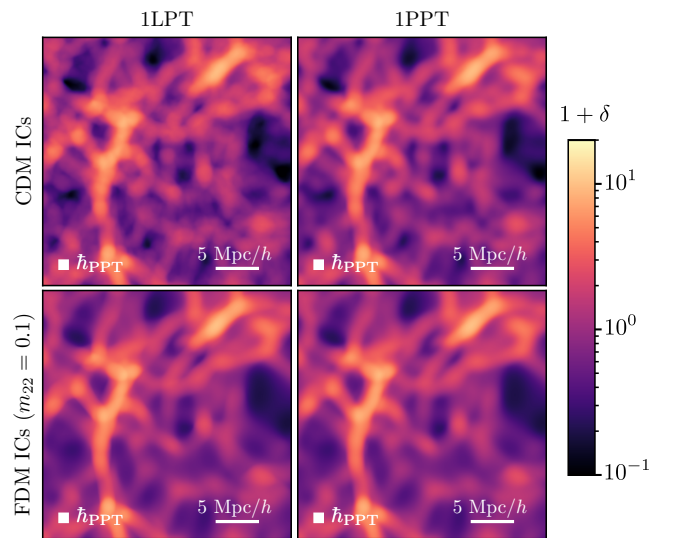


Figure 15. Projected $0.125 \text{Mpc}/h$ slice of the dark matter density at $z = 4.0$, as in Figure 1, after the fields have been smoothed with a top-hat filter of radius $R = 1 \text{Mpc}/h$. These show the same region as the zoomed insets in Figure 1 and are shown on the same colour scale.

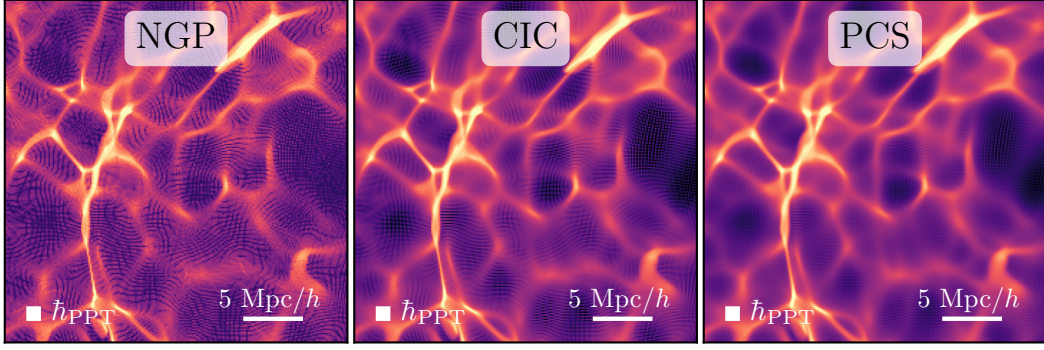


Figure 16. Density fields for 1LPT + FDM ICs as in Figure 1, where particle positions have been deposited on the grid by different mass assignment schemes: nearest grid point (NGP), cloud-in-cell (CIC), piecewise cubic spline (PCS). The fine grained crosshairs seen in the underdense regions disappear as the mass assignment order increases.

use the smoothed density field, such as that shown in Figure 15, where these fine grained patterns disappear in cloud-in-cell (CIC) assignment. We make use of CIC

mass assignment to construct density fields from LPT displacements throughout the rest of this work.